J. Fluid Mech. (1994), *vol.* 277, *pp.* 23–54

Turbulent penetration of a thermally stratified interfacial layer in a wind tunnel

By JAYESH† AND Z. WARHAFT
Sibley School of Mechanical and Aerospace Engineering, Cornell University, Ithaca,
NY 14853, USA

(Received 10 September 1993 and in revised form 25 April 1994)

A stably stratified interface, with strong turbulence below and quiescent air above, is studied in a wind tunnel with the aim of simulating the conditions at the inversion cap at the top of the atmospheric boundary layer. The interfacial layer was generated by means of a composite grid, with small mesh size above and a large one below (Veeravalli & Warhaft 1989). A temperature step generated in the plenum of the wind tunnel, was located at the centre of the layer. There is no shear and thus turbulence interactions, usually masked by turbulent production in traditional mixing layers, are highlighted. Close to the grid where the velocity fluctuations are strong, buoyancy effects are insignificant, but as the turbulence decays they become dominant. The bulk Richardson number, $N_B^2/(\langle u^2\rangle_2/L_u^2)$, where N_B is the Brunt–Väisälä frequency across the layer, and $\langle u^2\rangle_2$ and L_u are the velocity variance and integral lengthscale, respectively, of the turbulence on the lower side of the layer, varied from approximately zero close to the grid to 80 far downstream. The stratification inhibited the turbulent penetration into the layer, reducing the high skewness and kurtosis of the velocity field for the neutral case, to Gaussian values. The layer, which initially thickened with downstream distance, thinned when buoyancy became pronounced, owing to the collapse of the heat flux. Significant regions of countergradient heat flux, and reversals in sign of the triple moment transport terms were observed in the upper part of the layer. An analysis of the value of the heat flux conditioned on the temperature fluctuations, showed that the large temperature fluctuations associated with weak turbulence became affected by stratification first. Cospectral analysis shows that these fluctuations are associated with large scales. We also show that although the joint normal approximation between velocity and temperature fluctuations is sound for a passive scalar field, it becomes less good with the onset of stratification, failing completely when the stratification is strong.

1. Introduction

The inversion cap, or interfacial layer at the top of the atmospheric boundary layer, plays an important role in the lower atmospheric dynamics, as well as inhibiting the rates of vertical transport of scalars such as temperature, humidity, carbon dioxide and pollutants to regions aloft (Turner 1973; Nieuwstadt & Van Dop 1982; Venkatram & Wyngaard 1988). The layer, characterized by a sharp vertical increase in mean temperature with a concomitant decrease in turbulence intensity (Caughey 1982 and figure 1), increases in its height above the ground during the day as the convective activity transports heat and momentum vertically upwards, eroding the nocturnal inversion of the night before. Typically, by the afternoon it is approximately 1 km

---

† Jayesh died in an accident on June 17, 1994.

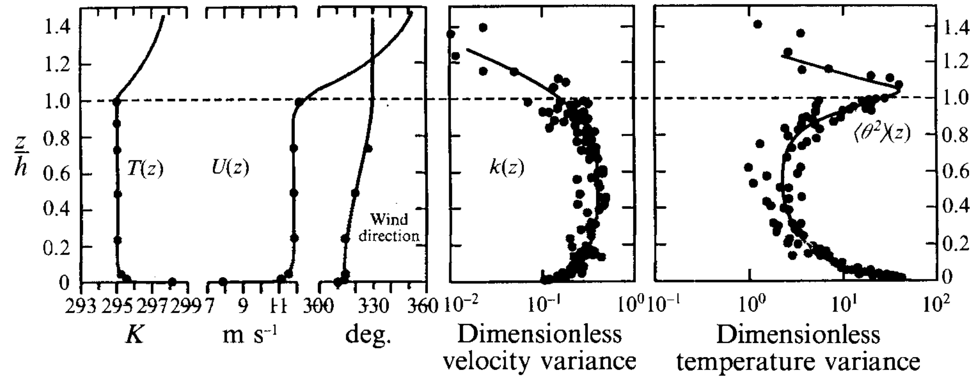

FIGURE 1. Typical vertical profiles of mean temperature ($T(z)$), wind speed $U(z)$, and wind direction, turbulence kinetic energy ($k(z)$), and temperature variance ($\langle\theta^2\rangle(z)$) as a function of height in the atmospheric boundary layer. The region of interest in the present work is the inversion at $z/h \sim 1$, where h is defined as the boundary-layer depth. Note that $k(z)$ and $\langle\theta^2\rangle(z)$ have logarithmic ordinates. From Caughey (1982).

above the ground. The interfacial layer can be clearly seen when ascending in an airplane from a polluted city (or for instance from atop the Acropolis in Athens), since the inversion locks the smog and particulates below, providing a demarcation between the polluted air and the clear blue sky above. While the broad characteristics of the interface are well documented, particularly the mean profiles of temperature, velocity, and turbulence intensity (Caughey 1982), and significant insight into the dynamics has been provided by modelling (Zeman & Lumley 1976; Zeman & Tennekes 1977; André *et al.* 1978), details of the transport processes are lacking. This is because the layer evolves with time, and is rarely observed in its ideal form, stripped of the complexities of underlying and surrounding terrain, making detailed *in situ* measurements very difficult. Indeed, Wyngaard (1973) has shown that the sampling time required to obtain satisfactory statistics of second-order quantities such as heat and momentum flux in the stably stratified atmosphere is longer than the layer lifetime. For these reasons there are no reliable measurements of higher-order statistics such as the probability density function (p.d.f.) of velocity and temperature as well as their conditional statistics, and the effect of large-scale intermittency on transport in the stable stratification is poorly understood. The layer, simple to describe in its broad outline, is rich and complex in its dynamics and transport characteristics, involving multiple lengthscales, intermittent penetration and buoyancy.

Our objective in the experiment to be described here, is to study in a wind tunnel, an essential characteristic of the inversion cap: large-scale energetic turbulence penetrating into an inversion with relatively quiescent air above. The way we have realized the flow is shown in figure 2. A mean temperature step formed in the plenum of the wind tunnel (upstream of the grid) passes through a composite grid which generates large-scale, energetic turbulence in the lower half of the tunnel and weak, small-scale turbulence above. The grid solidity (close to open area ratio) is constant throughout, such that there is no shear. Thus there is an interface of large- and small-scale turbulence, a turbulence mixing layer (Veeravalli & Warhaft 1989). The stratified interface is adjusted so that it is at the centre of the mixing layer. Downstream of the grid there results the mean profiles shown in figure 2. These profiles should be compared with those of the real inversion cap shown in figure 1. While the mean temperature, temperature variance and velocity variance are qualitatively similar, there are some significant differences. First, we have chosen not to have shear since this

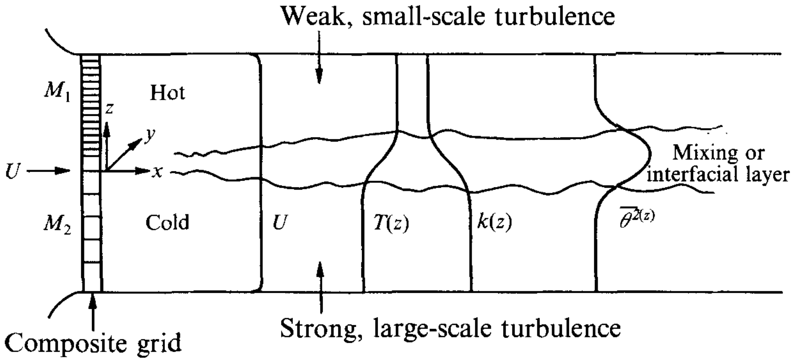

FIGURE 2. A sketch of the test section of the stratified wind tunnel showing vertical profiles of U, $T(z)$, $k(z)$ and $\langle\theta^2\rangle(z)$. The composite grid (Veeravalli & Warhaft 1989) generates large-scale turbulence at the bottom, and small-scale turbulence above, in the absence of mean shear. The temperature step is generated to the left of the grid in the plenum chamber by means of a number of horizontal heating rods, the bottom half of which are turned off (Yoon & Warhaft 1990). The profiles of mean temperature, kinetic energy and temperature variance in the mixing or interfacial layer should be compared with those at $z/h \sim 1$ of figure 1.

causes turbulence production which masks the transport processes and dominates the dynamics. While shear often occurs at the interfacial layer, it is not essential to its structure and evolution, and capping inversions are quite frequently observed in its absence. Secondly, the underlying, large-scale turbulence which penetrates the layer is mechanically, and not convectively driven. In the atmosphere both mechanical and convective turbulence occur, the latter often dominating the interfacial dynamics. The most serious drawback of generating the mechanical turbulence by a grid is that, as will be shown below, the large-scale turbulence is of approximately the same size as the depth of the capping inversion since it controls its dynamics, while in the atmosphere the size of the largest convective eddies are very large compared to the interfacial layer depth (although somewhat smaller eddies are responsible for the energetics at the interface). Thus we cannot claim to be actually mimicking the interfacial layer, even in its ideal form. We do hope, however, to be able to add insight into some of its salient characteristics.

Wind-tunnel experiments have the advantage of being controlled and statistically stationary in time at a particular measurement location of the flow, and thus there are no limits to the sampling time required to obtain higher-order statistics. This overcomes a primary obstacle not only of *in situ* measurements but also of grid stirred experiments (Turner 1973; Crapper & Linden 1974; Linden 1979; Dickey & Mellor 1980; Britter *et al.* 1983; Browand & Hopfinger 1985; Hopfinger 1987; Ruddick, McDougall & Turner 1989; Fernando 1992) where a stirring grid excites an initially quiet fluid and as time evolves the flow changes. While these laboratory experiments have provided significant insight into the overall dynamics and transport characteristics of interfacial layers, they too have not been able to provide data on the higher-order statistics and thus the details of the flow structure.

The present experiment may be viewed as a combination of our previous experiments on the turbulence mixing layer (Veeravalli & Warhaft 1989, 1990) and the experiments done by Jayesh, Yoon & Warhaft (1991) of a stably stratified step in conventional grid generated turbulence. In the turbulence mixing-layer experiments, where large-scale energetic turbulence was generated in the lower half of the tunnel and weak, small-scale turbulence was generated above it (but in the absence of stratification), Veeravalli &

Warhaft (1989) showed that the layer, formed between the two regions of homogeneous turbulence, thickened owing to a combination of intermittent large-scale penetration and turbulence diffusion†. On the other hand the experiments done by Jayesh *et al.* (1991) were for uniform turbulence intensity formed by a conventional biplanar grid. A stably stratified temperature step was imposed and the heat-flux in the middle of the layer collapsed by the action of buoyancy as the flow evolved. This caused a thinning of the layer with downstream distance as opposed to thickening that is observed in the passive case (Ma & Warhaft 1986). In the present work, we imposed a stratified temperature step at the centre of the turbulence mixing layer. We will show that the turbulent penetration observed for the passive mixing layer by Veeravalli & Warhaft (1989) is suppressed and as the flow evolves the flux collapses in a similar manner to the grid experiment of Jayesh *et al.* (1991). However, here the flux is negligible in the top half of the layer because the turbulence intensity is very small, and there is a range of turbulence intensities and lengthscales inside the layer, which introduce different levels of stability effects. Thus there is a distinct asymmetry across the layer in contrast to the situation observed by Jayesh *et al.* (1991) in their thermally stratified interfacial layer where the turbulence intensity was the same on both sides.

The governing equation for the mean temperature, T, is

$$U\frac{\partial T}{\partial x} = -\frac{\partial \langle \theta w \rangle}{\partial z}. \tag{1}$$

The angled brackets indicate averaging (for the present work time averaging), U is the mean velocity, θ is the fluctuating temperature and w is the fluctuating vertical velocity. The vertical direction is z (see figure 2) and the mean flow direction is along the x-axis. The molecular diffusion term has been omitted since even in a relatively low-Reynolds-number flow such as this, it is negligible compared to the turbulence transport term. For a passive thermal mixing layer, Ma & Warhaft (1986) have shown that the temperature step causes a negative (down-gradient) heat flux, with its maximum magnitude at the centre of the mixing layer and asymptoting to zero at its edges. Equation (1) then shows that the negative flux divergence will cause the layer to thicken with downstream distance, since $\partial T/\partial x$ is negative above and positive below the centreline, and this was observed to be the case from the evolution of the mean layer half-width. For the present case, close to the grid the turbulence is very energetic, and hence in spite of the imposed temperature (density) step, inertial forces dominate and the flow is close to passive. Thus thickening will occur here too, primarily in the lower portion where there is highly energetic turbulence. However, as the flow evolves, the vertical heat flux may collapse and even change sign owing to stratification. If the collapse of the heat flux in the layer leads to a change in the sign of the flux divergence (which will certainly be the case if there is countergradient heat flux in the layer, because the flux is zero outside the layer) then thinning of the layer will occur (equation (1)). This was observed in the stably stratified step experiment of Jayesh *et al.* (1991) and we will show this to be the case here too (§3.3.2 below).

The kinetic energy equation for the flow is

$$U\frac{\partial k}{\partial x} = \frac{g}{T_0}\langle \theta w \rangle - \epsilon - \frac{\partial \langle kw \rangle}{\partial z} - \frac{1}{\rho_0}\frac{\partial \langle pw \rangle}{\partial z}. \tag{2}$$

---

† Since we reported our earlier work we have become aware of a similar experiment by a Russian group (Aleksenko, Bukreev & Kostomakha 1984). Apparently Gilbert (1980) was the first to study this type of flow, but as we have previously noted, large-scale penetration was absent in his flow because the turbulence ratio was too small.

Here $k = 1/2\langle u^2+v^2+w^2\rangle$, where u, v and w are the fluctuating velocities in the x-, y- and z-directions (see figure 2), p is the fluctuating pressure, θ is the fluctuating temperature, g is the acceleration due to gravity, ϵ is the dissipation rate of fluctuating kinetic energy by viscosity and T_0 and ρ_0 are the reference temperature and density, respectively (taken here as the average of the upper and lower homogeneous regions). In the stably stratified experiment carried out in homogeneous turbulence (Jayesh *et al.* 1991), the turbulence kinetic energy was slightly depleted in the middle of the layer by the action of buoyancy and thus there was a small amount of transport of kinetic energy to the centre of the layer. In this experiment, owing to our imposed initial conditions, there is a vertical gradient in kinetic energy (figure 2) and hence the transport of kinetic energy will be a dominant term. Notice that there is no mechanical production term in (2) since there is no shear. The only possibility of production is if a counter-gradient heat flux occurs and the sign of the flux term, $(g/T_0)\langle\theta w\rangle$ changes from negative to positive. The reader is referred to Veeravalli & Warhaft (1989) for a detailed discussion of the energetics of the shearless mixing layer in the absence of stratification.

The scalar variance and scalar flux equations are (e.g. Townsend 1976),

$$U\frac{\partial(\frac{1}{2}\langle\theta^2\rangle)}{\partial x} = -\langle\theta w\rangle\frac{\partial T}{\partial z} - \epsilon_\theta - \frac{\partial(\frac{1}{2}\langle\theta^2 w\rangle)}{\partial z}, \tag{3}$$

$$U\frac{\partial\langle\theta w\rangle}{\partial x} = -\langle w^2\rangle\frac{\partial T}{\partial z} + \frac{g}{T_0}\langle\theta^2\rangle - \frac{1}{\rho_0}\left\langle\theta\frac{\partial p}{\partial z}\right\rangle - \frac{\partial\langle w^2\theta\rangle}{\partial z}. \tag{4}$$

Here ϵ_θ denotes the destruction rate of temperature fluctuations by molecular smearing. In the scalar variance equation $\partial\langle\theta^2 w\rangle/\partial x$ has been neglected since this should be very small compared to the leading terms. Similarly in the scalar flux equation $U\partial\langle\theta w\rangle/\partial x$, $(\alpha+\nu)\langle(\partial\theta/\partial x_i)(\partial w/\partial x_i)\rangle$, $\partial\langle\theta uw\rangle/\partial x$ and $\langle uw\rangle\partial T/\partial x$ have been omitted. Here α and ν are the thermal diffusivity and kinematic viscosity, respectively. Note that normally in a stably stratified situation, the flux will take energy from the kinetic energy via $(g/T_0)\langle\theta w\rangle$ (equation (2)) and feed it to the potential energy via the $-\langle\theta w\rangle\partial T/\partial z$ term in (3). (The potential energy is $(g/T_0)(\langle\frac{1}{2}\theta^2\rangle/\beta)$, i.e. it is proportional to $\langle\theta^2\rangle$ and thus (3) is proportional to the fluctuating potential energy. See (4) of Yoon & Warhaft (1990) and related discussion.) However, as can be seen from (4), the heat flux can change sign if the second term on the right-hand side becomes more dominant than the first term, and in that case the production term in scalar variance equation becomes the sink term and the energy is put back into the kinetic energy from potential energy. We will consider the details of the interactions of the various terms in the budget equations below and compare them to the more simple flows of Jayesh *et al.* (1991) (stratified step) and Yoon & Warhaft (1990) (linear mean density profile) in conventional grid turbulence.

While in reporting our results we will describe the bulk characteristics of the flow and its downstream evolution (§§3.1 and 3.3.1), particular emphasis will be placed on the structure of the layer itself, especially far downstream where the stratification is strong. Thus we will examine the probability density function of the velocity fluctuations (§3.2), the transport of heat and temperature variance within the layer, and the conditional heat flux and the cospectra (§3.3). These results will be contrasted with the passive case and with simpler stratified flows. We believe that the stationarity of the flow, and our ability to do high resolution, fast response measurements by means of hot-wire anemometry, has provided favourable conditions for the study of these

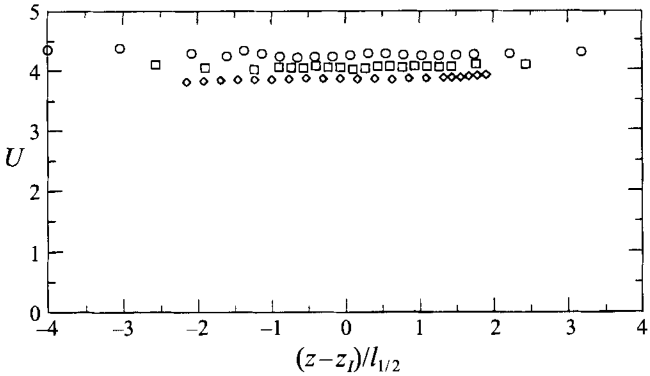

FIGURE 3. Mean vertical velocity profiles. ○, $x/M_2 = 19$; □, $x/M_2 = 32$; ◇, $x/M_2 = 146$. The vertical height has been normalized by the inflexion height of the velocity profile, z_I, and the layer half width $l_{1/2}$ (see §3). The slight variation of the average value from the nominal value of 4 m s^{-1} is not a downstream trend, but owing to the measurements being carried out on different days. (During a particular run $U(z)$ was constant (within a few percent) with downstream distance.)

higher-order statistics. As mentioned above, this information has not been provided by *in situ* measurements or by laboratory grid stirred water tanks.

2. Apparatus

We performed the experiment in our large (0.91 × 0.91 m^2 and 9.1 m long) open circuit, low turbulence level (less than 0.25% turbulence intensity without grid), suction wind tunnel designed specially to study stratified flows. A detailed description of the wind tunnel is given in Yoon & Warhaft (1990). A schematic diagram of the experimental set-up is shown in figure 2. A grid with two different mesh sizes on top and bottom but the same solidity throughout was used to create turbulence of the nature described in §1. The grid design was essentially that of Veeravalli & Warhaft (1989, 1990) but was rescaled to fit the stratified horizontal tunnel used in our present experiment. (Veeravalli & Warhaft 1989, 1990 used a vertical wind tunnel of smaller cross-section (0.406 × 0.406 m^2).) On the top half of the flow (i.e. the low-turbulence region) a rectangular wire mesh screen (wires in both vertical and horizontal direction) of mesh size 3.175 mm and wire-diameter 1.19 mm with open area of 60.2% (or solidity of 29.8%) was used; on the bottom, horizontal parallel adjustable bars of width 11.11 mm were used. Here too the solidity was 29.8%. Thus the ratio of the large- to small-scale mesh sizes, M_2/M_1 was 12.6, a value higher than in our previous work. Shimming blocks were employed on the large mesh side to avoid the large-scale inhomogeneity in the flow (Veeravalli & Warhaft 1989). Thoroddsen & Van Atta (1993) have shown that the grid configuration does not play any dominant role in the evolution of turbulence in a stably stratified flow, be it formed by a rectangular mesh or vertical or horizontal bars, hence the fact that the top portion is a wire mesh (essentially biplanar-grid), whereas the bottom portion is a parallel-bar grid, should have no effect on the nature of the results to be described here. A long trial and error method was employed to fine tune the grid to produce the desired condition of no shear with a step in turbulence intensity. Figure 3 shows the mean velocity profile at three downstream locations. The overall change in U is less than 5% across the flow, comparing favourably with that observed by Veeravalli & Warhaft (1989). Note that

(a) $\frac{x}{M_2}$	U (m s^{-1})	$\langle u^2\rangle_2/U^2(\times 10^2$ m s$^{-1})$	$\frac{z_I}{M_2}$	$l_{1/2}$ (cm)
12.67	4.01	1.084	12.17	0.831
19.00	4.27	0.585	12.25	1.323
25.34	3.95	0.458	12.16	1.335
31.67	4.06	0.334	11.84	1.898
145.69	3.86	0.047	13.79	2.730

(b) $\frac{x}{M_2}$	ΔT (°C)	U (m s^{-1})	Ri_B	N_B	Fr_B	$\frac{\langle u^2\rangle_2}{U^2}$ ($\times 10^2$)	$\langle\theta^2\rangle_{max}$ (°C^2)	$\frac{z_c}{M_2}$	$\frac{z_I}{M_2}$	$\frac{z_{max}}{M_2}$	$\frac{l_T}{M_2}$	$\frac{l_{1/2}}{M_2}$	$\frac{l_\theta}{M_2}$	$\frac{L_u}{M_2}$	η (mm)	Re_l
12.67	10.88	4.45	0.08	3.17	35.04	1.002	4.14	12.09	12.00	11.34	0.859	0.858	0.808	1.013	0.22	1062
19.00	9.91	4.54	0.22	3.14	36.01	0.531	4.24	12.42	12.21	11.66	0.796	1.248	0.837	1.247	0.29	975
25.34	10.32	4.61	0.65	2.97	38.72	0.400	3.99	12.54	12.15	11.63	0.933	1.686	1.057	1.968	0.35	1366
31.67	10.34	4.71	0.77	2.97	39.58	0.274	3.73	12.58	12.26	11.64	0.933	1.641	1.056	1.816	0.39	1061
101.35	19.81	4.05	16.08	4.10	24.62	0.067	12.47	13.60	12.98	12.55	0.936	2.003	1.148	2.556	0.81	635
145.69	20.19	3.91	63.10	4.36	22.34	0.048	11.26	13.40	12.98	12.85	0.839	2.697	0.863	3.192	1.00	646
177.36	20.77	3.92	74.65	4.59	21.30	0.043	9.65	13.41	12.59	12.86	0.784	2.004	0.715	3.823	1.08	738
190.02	19.62	4.24	81.47	4.64	22.77	0.034	8.63	13.39	12.84	12.65	0.721	1.781	0.744	3.811	1.11	707

TABLE 1. Various bulk properties of the flow for the cases without a temperature step (*a*) and with a temperature step (*b*). The nominal wind speed was 4.0 m s^{-1} for the passive case and for $\Delta T = 20$ °C and 4.5 m s^{-1} for $\Delta T = 10$ °C. Only one downstream location could be measured at a time (each x/M_2 location took ~ 5 h). Thus in tuning the profile each day, ΔT and U varied slightly. The nominal temperature steps used were $\Delta T = 10$ °C and 20 °C (these are separated by a space in (*b*)). The mesh Reynolds number, $Re_M \equiv UM_2/\nu$ for the lower region of the flow was ~ 11000. The turbulence Reynolds number defined for the strong turbulence side of the flow outside the interfacial layer, which is passive, is $Re_l \equiv \langle u^2\rangle_2^{1/2} L_u/\nu$ and the bulk Froude number is defined as $Fr_B \equiv U/(N_B M_2)$. N_B, the Brunt–Väisälä frequency is defined as $((g/T_0)(\Delta T/l_T))^{1/2}$. The length η is the Kolmogorov scale. The velocity decay law for the large scale flow below the mixing layer is $\langle u^2\rangle/U^2 = 0.25(x/M_2)^{-1.33}$

the interface of the large and small scale is at $z = z_I$. We have calculated that the maximum shear production by the inhomogeneities in the mean gradient is less than about 10% of the dissipation, again this is comparable to the results of Veeravalli & Warhaft (1989). The turbulence intensity profiles will be discussed in §3.1.

Heating elements at the entrance of the plenum (Yoon & Warhaft 1990, figure 1) were employed to produce the desired temperature step. Measurements were made for nominal values of $\Delta T = 10$ °C and 20 °C. The resulting Richardson numbers, Froude numbers, etc. are given in table 1. Setting up the temperature profile involved repeated experimental trials in adjusting the voltages of each of the elements separately. The mean temperature profiles thus obtained will be discussed in §3.1.

In order to tune the mean temperature profile and measure its evolution, temperature measurements were made using an array of Chromel–Constantan thermocouples. The mean velocity, fluctuating velocities and fluctuating temperature were measured using an X-wire in conjunction with a cold wire. The calibration procedure for the X-wire was similar to that of Champagne & Sleicher (1967), and is described in Yoon & Warhaft (1990). The mean voltage from the cold wire was also used to determine the mean temperature profile simultaneously with the fluctuations. Wollaston wires of 5.08 μm diameter were used for the X-wire with the length to diameter ratio approximately 200, and the over heat ratio 1.95. A platinum resistance wire of 1.27 μm with length to diameter ratio of 400 was used for the cold wire. Dantec 55M01 constant temperature bridges were used in conjunction with the X-wire and for the cold wire, a d.c. fast response temperature bridge based on the design of Haughdal & Lienhard (1988) was used. The measurement procedures were the same as Jayesh *et al.* (1991). All three channels were filtered and amplified using Krohn Hite model 3342 filters and were then digitized and stored with a resolution of 12 bits in a MicroVaxII for subsequent data analysis. For the estimation of spectra, the sampling frequency per channel was set at twice the Nyquist frequency (3–10 kHz depending on the tunnel speed) and 10^5 data points were used for the estimates of these quantities. For the determination of the p.d.f.s and related quantities, 10^5 data points were also used but the sampling rate was slower (typically 425 Hz) so that independent samples could be obtained.

We took smoke-wire photographs to aid our qualitative understanding of the flow using a similar procedure to that of Jayesh *et al.* (1991). The wire was placed vertically, in the centre of the flow, at $x/M_2 = 152$ and the camera was placed $19M_2$ downstream of the smoke-wire. High speed (ASA 3200) black and white film was used. The shutter was kept open for a comparatively long time (the inside of the wind tunnel was sealed from light), and the flow was frozen using one primary electronic flash-unit which triggered two subsidiary, light-sensitive flash units. The flashes were placed inside a box which was designed to let out a thin sheet of light, and a thin strip of mirror was placed on the top and bottom wall of the tunnel to reflect the light coming from the flash-box to make the field of view well lit. The primary flash-unit and camera-shutter, and the heating of the smoke-wire was controlled using a home made electronic package in conjunction with the device driver of the MicroVaxII. The flash-delay (time elapsed between the heating of the smoke-wire and the triggering of the camera-flash unit) and the aperture (big apertures were generally used, since the depth of field was not an issue: smoke was only in a very thin sheet, with thickness less than $u'19M_2/U$, which is of the order of 15 mm) was varied over a wide range to capture the flow with best 'colouring'. Oil used to coat the smoke wire was SAE 20W50, and the current and voltage were 6 A and 60 V, respectively.

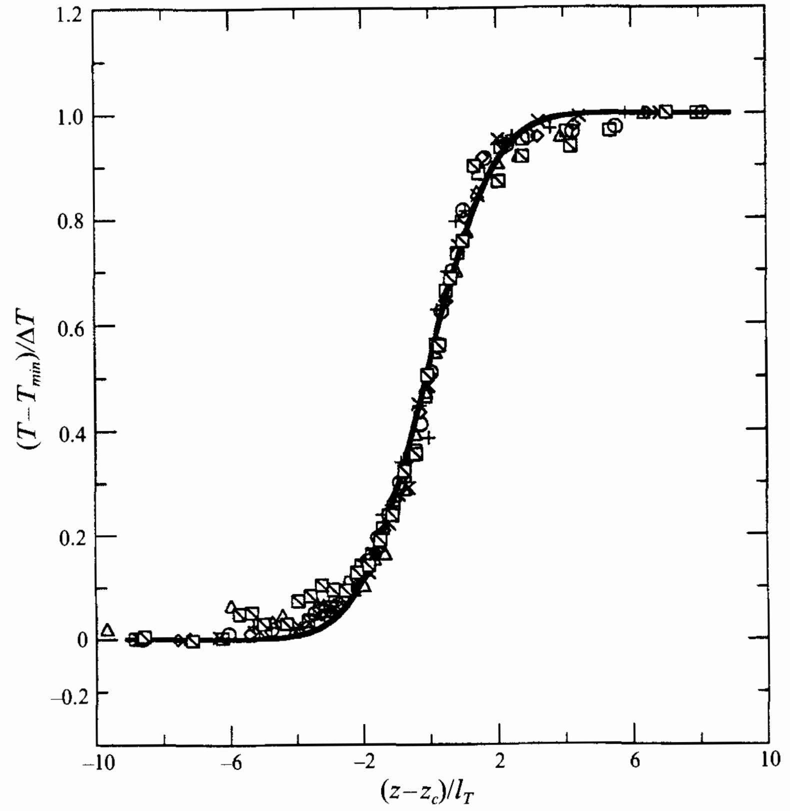

FIGURE 4. Mean temperature profiles normalized by the temperature step, ΔT. T_{min} is the ambient temperature in the large-scale turbulence region. The height z is normalized by the mean thermal half width l_T (see table 1 and text for definition). z_c is the centreline height of the mean temperature profile. ○, $x/M_2 = 25$; □, $x/M_2 = 38$; ◇, $x/M_2 = 51$; ×, $x/M_2 = 76$; +, $x/M_2 = 101$; △, $x/M_2 = 152$; ⧄, $x/M_2 = 177$; solid line, best fit error function.

3. Results

3.1. *Flow realization and bulk characteristics*

The ideal initial conditions for this flow are a positive step in mean temperature occurring at the centre of the interface of large- and small-scale turbulence, in the absence of a mean velocity gradient. As we have shown in §2, the mean velocity is indeed very close to constant across the layer, with variations of less than a few percent. However, because of the very complex motion close to the grid (up to approximately 30 mesh lengths (Jayesh & Warhaft 1992)) where there are a series of coalescing wakes downstream of the grid bars, it is not possible to achieve such a simple initial condition for the thermal and velocity variance fields. Thus although the temperature step is approximately realized in the plenum chamber, at the grid the turbulence causes spreading, and by the time the velocity variance field becomes well conditioned, the mean temperature profile has assumed an approximate error function shape. We began our measurements at approximately $13M_2$ lengths downstream of the grid, where M_2 is the mesh length of the large-scale grid (the lower part of the flow, figure 2). At this location the turbulence in the upper part of the flow has almost completely decayed since here the downstream location is at $x/M_1 \sim 165$. Table 1 lists the parameters for the flows we have studied in detail.

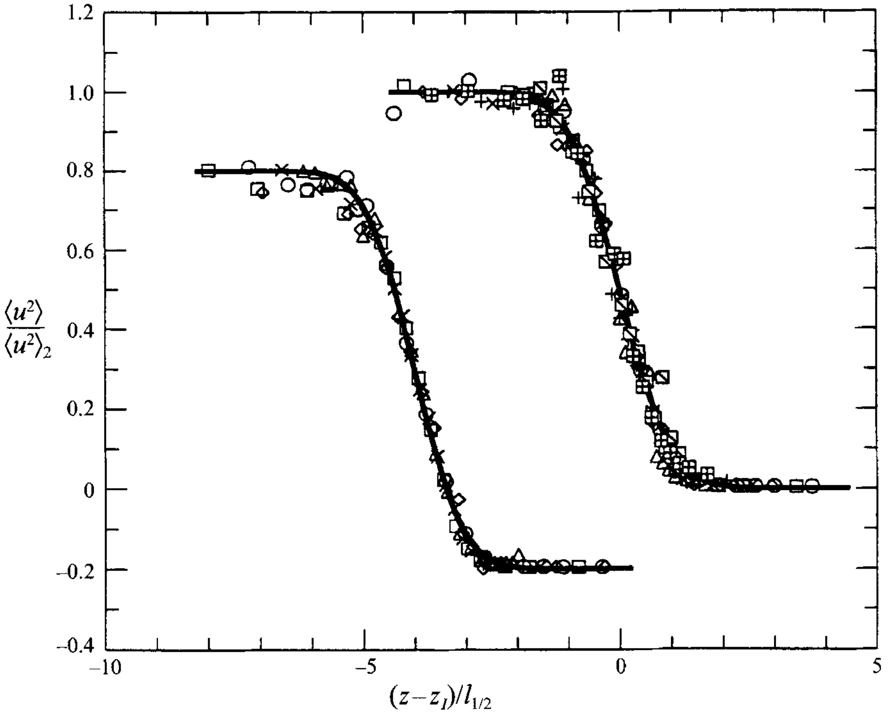

FIGURE 5. Horizontal velocity variance profiles, without stratification (left-hand side) and with stratification (right-hand side). $\langle u^2\rangle_2$ is the velocity variance in the strong turbulence side of the layer, $l_{1/2}$ is the velocity half width of the layer (table 1 and text) and z_I is the inflexion height of the velocity variance profile. ○, $x/M_2 = 13$; □, $x/M_2 = 19$; ◇, $x/M_2 = 25$; ×, $x/M_2 = 32$; +, $x/M_2 = 101$; △, $x/M_2 = 146$; ⧄, $x/M_2 = 177$; ⊞, $x/M_2 = 190$; solid line, best fit error function. The profile on the left has been shifted -4 non dimensional units to the left and down by -0.2 units.

Figures 4 and 5 show the vertical mean temperature and horizontal velocity variance profiles normalized by the half widths at the particular downstream measurement location (the way we determined the half width is outlined below). In spite of the fact that buoyancy becomes more significant with downstream distance, all the profiles appear to collapse well as an error function. This was also the case for the vertical velocity variance profiles (not shown). We will show below that there is in fact slight asymmetry, particularly in the mean temperature profiles. The asymmetry of the layer will become strikingly evident when we discuss the higher-order moments below.

The evolution of the layer half width, l_T, is shown in figure 6. Here l_T is defined as half the distance between the z-locations, where the values of the normalized temperature are 0.25 and 0.75, respectively. The normalized temperature is defined as $T^* \equiv (T-T_{min})/\Delta T$, where $\Delta T = T_{max}-T_{min}$ and T_{min} is the temperature of the lower half of the flow and T_{max} is the temperature of the upper half of the flow, i.e. they are the minimum and maximum temperature that exist in the flow. It is evident in figure 6 that the half width first increases as would be expected for a passive temperature step, and then owing to the stabilizing effect of the layer, it becomes thinner. The same phenomenon was observed by Jayesh *et al.* (1991). In the present flow, however, the top half-width, l_{T1} (the distance between the z-location where the value of T^* is 0.5 to where it is 0.75) does not change much, because the flow in the top half has negligible turbulence, and thence negligible flux, as compared to the flow in the lower part of the layer. On the other hand, the bottom half-width, l_{T2}, (the distance between the z-

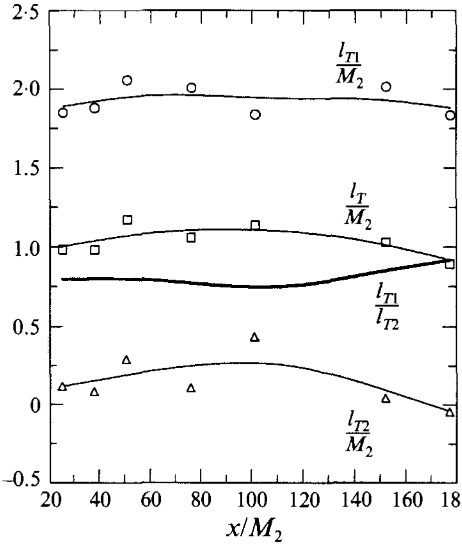

FIGURE 6. Downstream evolution of the half width of the mean temperature profile, l_T, and its partition for the upper part of the layer, l_{T1}, and lower part, l_{T2}, as well as their ratio, l_{T1}/l_{T2}. (See table 1 and text for definitions), M_2 is the mesh length of the large grid bars. □, l_T; ○, l_{T1}; △, l_{T2}; thick line, l_{T1}/l_{T2}. l_{T1} has been shifted up by 1.0 and l_{T2} has been shifted down by 1.0 on the vertical axis.

location where the value of T^* is 0.25 to where it is 0.5) first increases and then it decreases. Thus most of the layer thickening and thinning is due to the bottom half of the layer while the top part remains approximately constant. The ratio l_{T1}/l_{T2}, shown in figure 6, brings out the slight amount of asymmetry present in the mean temperature, which is not evident in figure 4. The ratio is approximately 0.8 initially, and then as the bottom half thickens the ratio becomes smaller. Finally, as the stratification becomes dominant the ratio increases towards unity. Here the flux in the high turbulence side is collapsing (see §3.3.2).

The increase followed by the decrease in the layer thickness (l_T/M_2, figure 6) is best understood in terms of the second-order equations and these will be discussed in §3.3.2, below. Here we note that in the grid-stirred tanks referred to in §1, the stratified interface is usually discussed in terms of the entrainment velocity. Thus, although our flow configuration is different, it is worth discussing our bulk flow characteristics in relation to these transient experiments. In order to express mixing in terms of entrainment at the interface, Linden (1979) suggests the expression

$$u_e/u \sim Ri_0^{-n}, \tag{5}$$

where u_e is the entrainment velocity, u is the characteristic turbulent velocity near the interface ($\langle u^2\rangle_2^{1/2}$ in our notation) and $Ri_0 \equiv [(g/T_0)(\Delta T/l_T)]/[\langle u^2\rangle_2/l_T^2]$. Note that Ri_0, the overall Richardson number, increases with x/M_2 primarily because $\langle u^2\rangle_2$ diminishes rapidly (see below). Expressing the mixing efficiency in terms of a flux Richardson number,

$$R_f = \frac{u_e}{u} Ri_0 = \frac{u_e g \Delta T l_T}{T_0 u^3}, \tag{6}$$

it follows from (5) and (6) that

$$R_f \sim Ri_0^{1-n}. \tag{7}$$

For $n < 1$, (7) implies R_f is an increasing function of Ri_0, and for $n > 1$, R_f is a decreasing function of Ri_0.

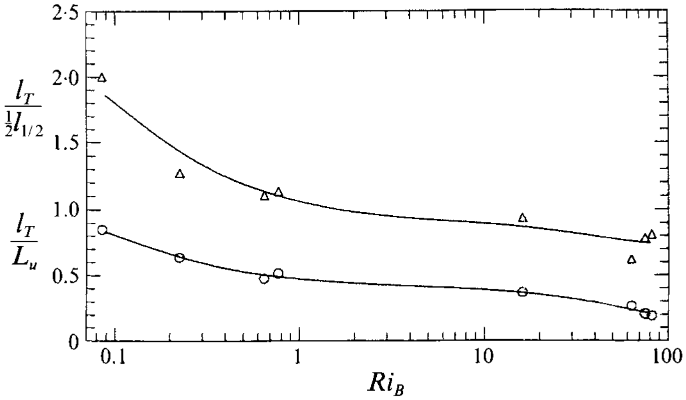

FIGURE 7. The mean temperature profile half width, l_T, normalized by both the mean velocity variance profile half width, $l_{1/2}$ (△), and also by L_u, integral lengthscale of the large-scale turbulence on the lower side of the layer (○). Ri_B is the bulk Richardson number (see text for definition).

Before attempting to express our results in terms of these relations, we note that there is a fundamental difference between the grid-stirred tank experiments and these reported here; for the latter the field is advected downstream and the turbulent penetration is normal to the advection velocity, whereas for the grid-stirred experiments the mixing and entrainment is in the same direction as the grid oscillations (and there is no mean flow). Nevertheless it is interesting to determine the relationship between R_f and Ri_0 for our flow also. By defining $u_e = \mathrm{d}l_T/\mathrm{d}t = U(\mathrm{d}l_T/\mathrm{d}x)$, and assuming a power law form for the layer thickness, i.e. $l_T \sim x^m$, it is evident from (5) that $n \lesseqgtr 1$ corresponds to $m \gtreqless -0.5$ (this value was determined using the velocity variance decay law, table 1). Using the data of figure 6, we find that for $x/M_2 < 100$, m has a slightly positive value and after the maximum, the value of m is slightly less than $-0.5(x/M_2 > 130)$. This, from the above, is consistent with an increasing and then decreasing value of R_f. Thus our result appears to be in qualitative agreement with the grid stirred tank experiments where it is found that a density gradient will thicken for small Ri_0 and after R_f has gone through a maximum, the density gradient becomes steeper (see for example Ruddick *et al.* 1989 and related work of Phillips 1972 and Posmentier 1977). We emphasize, however, the difference in boundary conditions of the two flows. Thus it is not clear whether the parameterization used in (7) is as useful for our flow as for the grid-stirred tanks. We also note that because of the scatter in figure 6, accurate determination of m is difficult.

In figure 7 we have plotted the evolution of the layer half-width normalized by L_u (lower points) and by $l_{1/2}$, the velocity variance half-width (upper points), both plotted as a function of Ri_B. Since the measurements were made on different days (each x/M_2 location took ~ 5 h) and the conditions were not precisely the same, we have not plotted evolution against downstream distance. Instead, following our earlier work (Jayesh *et al.* 1991) we have plotted the layer evolution in terms of the bulk Richardson number, which increases with downstream distance as the turbulence decays. The bulk Richardson number is defined as $Ri_B \equiv (g/T_0)(\Delta T/l_T)/(\langle u^2\rangle_2/L_u^2)$, where $\langle u^2\rangle_2$ is the longitudinal velocity variance on the strong turbulence side, and $L_u(\equiv \langle u^2\rangle_2^{3/2}/\epsilon)$ is the integral lengthscale on the strong turbulence side. It is closely related to Ri_0 (defined above) but now we are recognizing that the thermal scale is different to that of the velocity scale in stratified flows. The dissipation rate, ϵ, was calculated using the formulation suggested by Stillinger, Helland & Van Atta (1983) for stratified

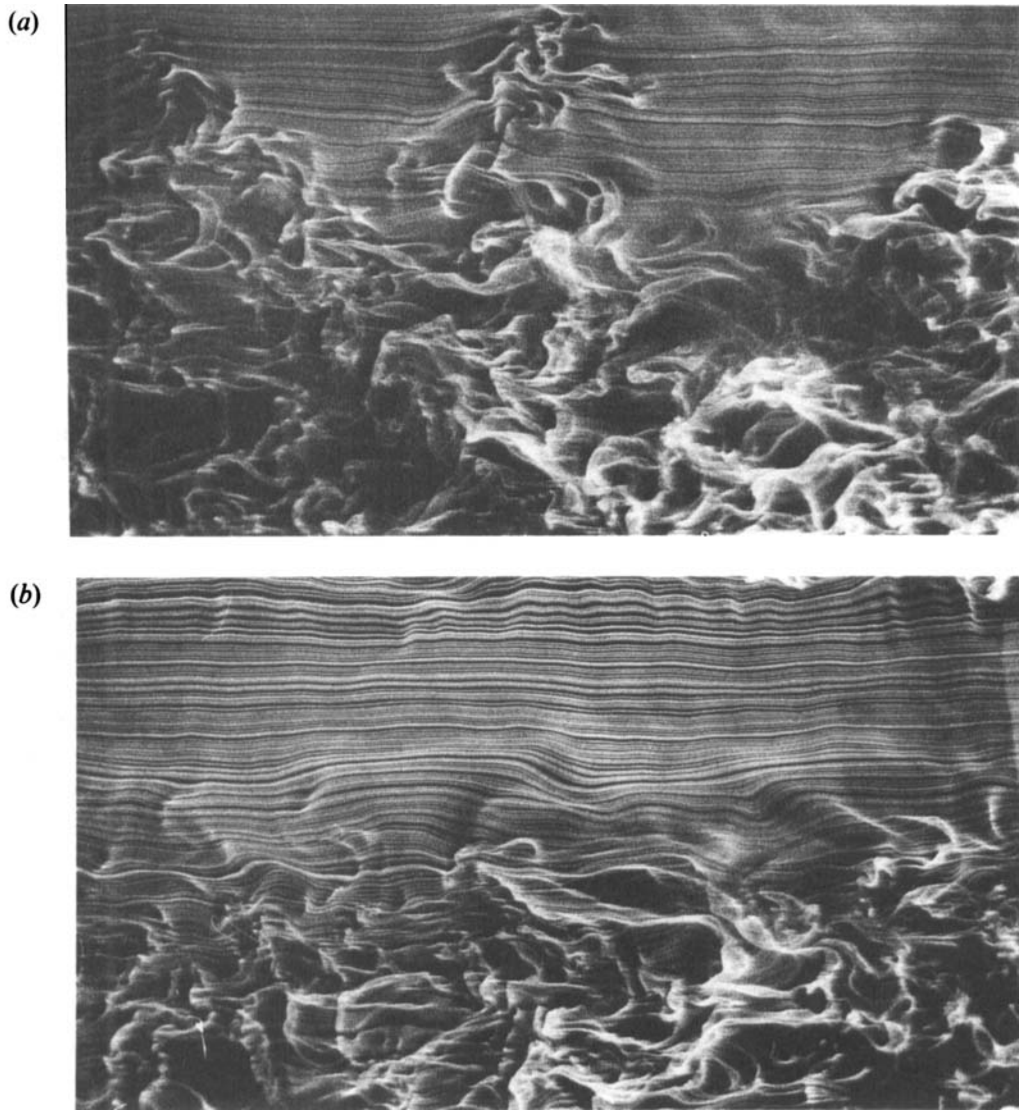

FIGURE 8. Smoke-wire visualization of the mixing layer without thermal stratification. (*a*); and with stratification, (*b*). Both photographs were taken at $x/M_2 = 171$ and the smoke was released at $x/M_2 = 152$. $U = 4\ \mathrm{m\ s^{-1}}$, $\Delta T = 20\ ^\circ\mathrm{C}$. The width of the field is 55 cm and its height is 30 cm.

turbulence: $\epsilon = \nu[10\langle(\partial u/\partial x)^2\rangle + 2.5\langle(\partial w/\partial x)^2\rangle]$. Here we have slightly modified the definition of Ri_B used by Jayesh *et al.* (1991); instead of using the centreline turbulence intensity and lengthscale we have used these parameters from the strong turbulence side. However, similar qualitative effects of buoyancy occur at approximately the same Ri_B using either definition. Veeravalli & Warhaft (1989) showed in their turbulence mixing-layer experiment that for mesh size ratio larger than 8:1, the layer dynamics is dominated by single lengthscale, which comes from the strong turbulence side. Thus for our flow, the velocity field is uniquely defined by L_u and $\langle u^2\rangle_2$. This is the reason for our particular choice of Ri_B for this flow. For the passive case in conventional grid turbulence, simple scaling suggests that the ratio l_T/L_u should remain constant, and this was shown experimentally to be the case (Ma & Warhaft 1986). However with

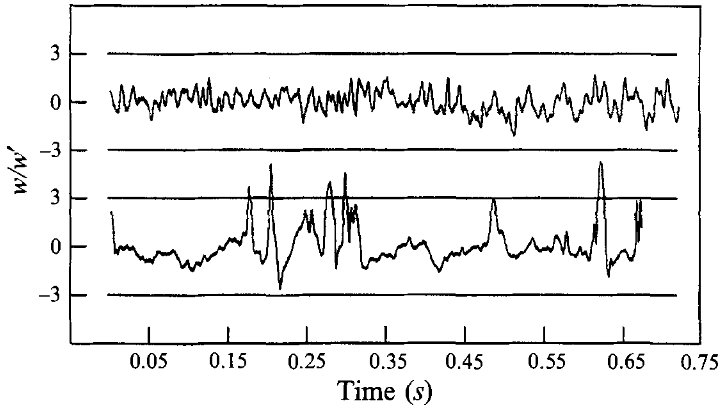

FIGURE 9. Time series of the vertical velocity fluctuations with stratification (upper series) and without stratification (lower series) at $x/M_2 = 146$; $z/M_2 = 17.1$ and $z/M_2 = 16.8$, respectively. The straight solid lines are ± 3 standard deviations from the mean.

stratification this ratio is reduced to less than half of its original value (figure 7). Browand & Hopfinger (1985) have shown that the vertical lengthscale is significantly reduced as compared to the integral lengthscale in stirred grid experiments, and their flow visualizations, showing horizontal fingers of dye protruding into the unmixed fluid, are a clear evidence of this fact. In the present experiment l_T is determined by the vertical lengthscale and the decrement in the ratio l_T/L_u reflects the same nature of stabilizing forces as was exhibited in the horizontal fingers of Browand & Hopfinger (1985). The ratio l_T/L_u is reduced by about the same degree as observed by Jayesh *et al.* (1991) in their thermal mixing-layer experiment in conventional grid turbulence. The upper points in figure 7 show $l_T/l_{1/2}$ as a function of Ri_B. The half width of the turbulence intensity profile, $l_{1/2}$ is defined as the distance between the points where the ratio of the maximum to minimum intensity is $\frac{1}{4}$ and $\frac{3}{4}$. Here, as for l_T/L_u, $l_T/l_{1/2}$ decreases with increasing stability. This implies that K_θ/K_u, the ratio of the thermal to momentum eddy diffusivities, is decreasing. A decrease of K_θ/K_u with increasing Ri has been observed in the atmospheric boundary layer (Wyngaard 1973), but the decrease is small compared with our experiment. The result can be explained by noting that all those fluid particles which carry a significant temperature deficit (or surplus) are inhibited by the stabilizing buoyancy force, whereas those which do not carry such deficit (or surplus) go unhindered.

3.2. *The velocity field*

Figure 8 shows the smoke visualization of the flow taken at $x/M_2 = 171$, with and without the stable stratification. Figure 8(*a*), with no stratification, shows excursions of large-scale turbulent eddies from below, which are penetrating into the essentially non-turbulent flow above. However, when the flow is stratified, i.e. the temperature step is turned on, these large excursions are suppressed owing to the action of buoyancy as shown in figure 8(*b*).

The suppression of the large eddies is evident from the time series of the vertical fluctuating velocity component. In figure 9 the bottom curve shows the time series with no stratification and the top curve shows the time series with the stratification. Both curves are taken at $x/M_2 = 146$ (in the intermittent region of the unstratified case). The intermittent bursts of high velocity are seen in the time series of unstratified case; with stratification these bursts are suppressed and there is no sign of intermittency.

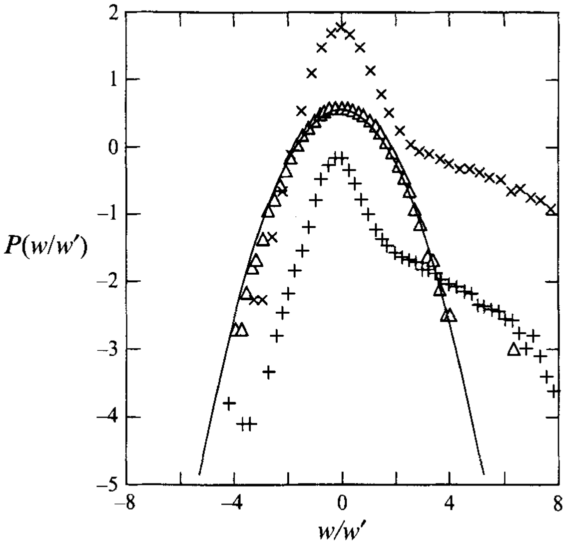

FIGURE 10. Probability density functions (p.d.f.s) of vertical velocity normalized by the local value of r.m.s. velocity, w'. All profiles were measured at $x/M_2 = 146$. △, with stratification at $z/M_2 = 17.1$; +, without stratification at $z/M_2 = 16.8$; ×, without stratification at $z/M_2 = 17.4$. The inflexion point of the profile is at $z/M_2 = 13.0$. The vertical axis is logarithmic and the solid line is a Gaussian p.d.f. The top two p.d.f.s are shifted up one and two decades, respectively.

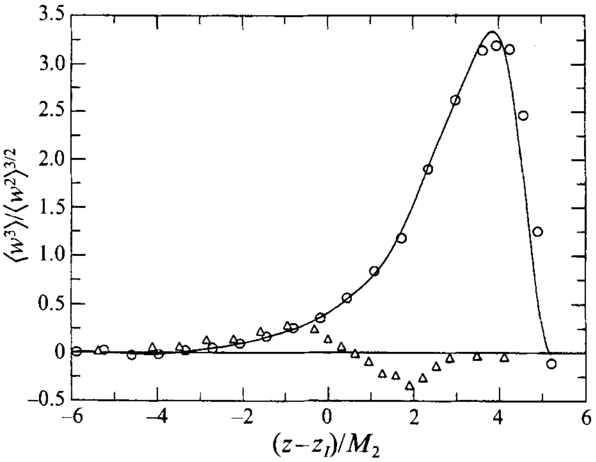

FIGURE 11. The profiles of the skewness of the vertical velocity fluctuations at $x/M_2 = 146$, with (△) and without (○) stratification ($\Delta T = 20.2$ °C).

The qualitative effects of the stratification observed in the time series (figure 9) manifest themselves by suppressing the long positive tail of the probability density function (p.d.f.) of the vertical velocity fluctuations. In figure 10, which shows the p.d.f. of vertical fluctuating velocity in the interfacial layer at $x/M_2 = 146$, the top and bottom curves are without stratification. The vertical axis is logarithmic in order to emphasize the details of the tails of the distribution. Note the stretched tails on the positive side of these curves indicating the large infrequent fluctuations of w. The middle curve is the p.d.f. with the stratification. A Gaussian p.d.f. is plotted for comparison and it is evident that the p.d.f. with the stratification is quite close to Gaussian. This, apart from showing that the large excursions are suppressed, suggests

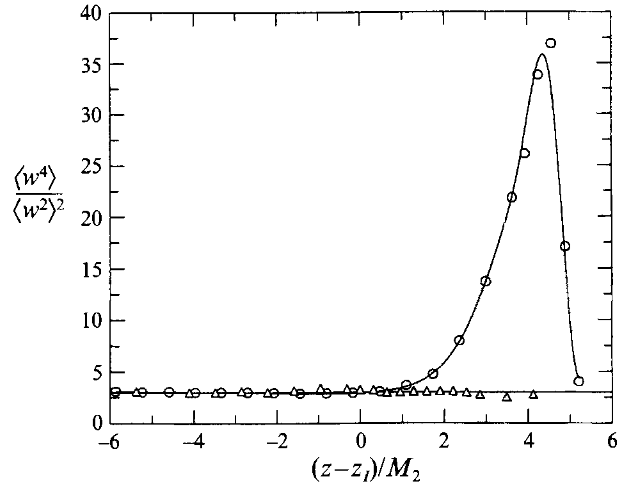

FIGURE 12. The profiles of the kurtosis of the vertical velocity fluctuations at $x/M_2 = 146$, with (△) and without (○) stratification ($\Delta T = 20.2$ °C).

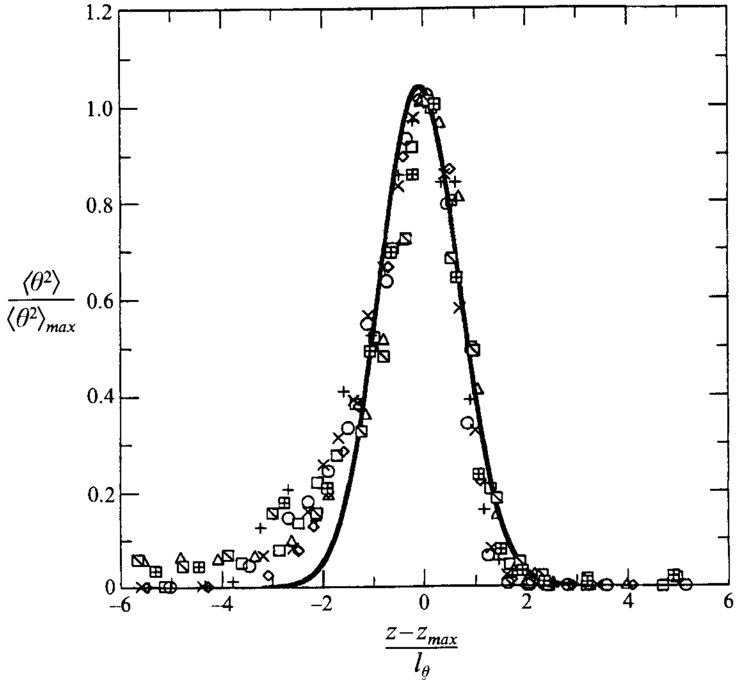

FIGURE 13. The vertical profiles of temperature variance normalized by their maximum value (where $z = z_{max}$). l_θ is the profile half width (see text for definition). The solid line is the best fit Gaussian. ○, $x/M_2 = 13$; □, $x/M_2 = 19$; ◇, $x/M_2 = 25$; ×, $x/M = 32$; +, $x/M_2 = 101$; △, $x/M_2 = 146$; ⧅, $x/M_2 = 177$; ⊞, $x/M_2 = 190$ (see table 1 for details on flow conditions).

that the transport of kinetic energy in the vertical direction must also be reduced by the action of buoyancy. We will show this to be the case below.

The extended tails of the p.d.f. (figure 10) for the unstratified case indicate a high positive value of skewness, $S \equiv \langle w^3\rangle/\langle w^2\rangle^{3/2}$. A plot of S, measured at $x/M_2 = 146$, is shown in figure 11. Near the bottom of the layer the turbulence is homogeneous and thus the skewness is zero. In the layer the skewness increases to a maximum and then

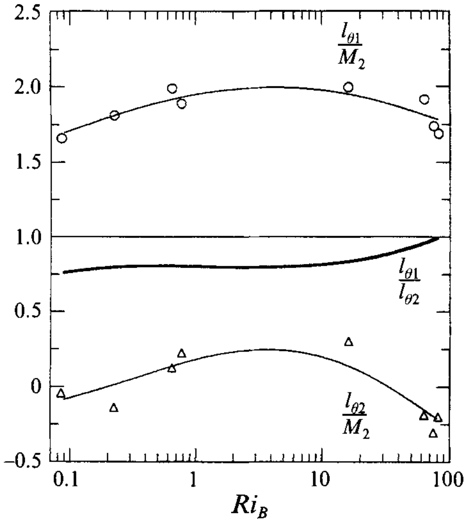

FIGURE 14. The half width of the temperature variance profiles of figure 13 plotted as a function of Ri_B. $l_{\theta 1}$ (○) is the half width of the upper portion of the profile and $l_{\theta 2}$ (△) is the half width of the lower portion. The solid line is the ratio, $l_{\theta 1}/l_{\theta 2}$. See text for definitions. $l_{\theta 1}$ has been shifted up by 1.0 and $l_{\theta 2}$ has been shifted down by 1.0.

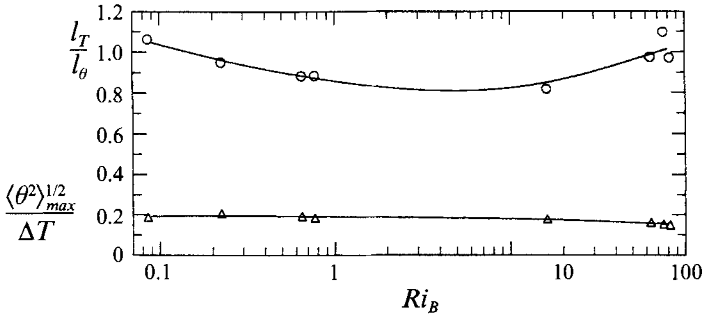

FIGURE 15. The ratio of the mean temperature profile half width to the temperature variance halfwidth, l_T/l_θ, and the ratio of the maximum r.m.s. temperature (at a particular x/M_2) normalized by the temperature step, plotted as a function of Ri_B. ○, l_T/l_θ; △, $\langle\theta^2\rangle^{1/2}_{max}/\Delta T$.

decreases back to zero towards the edge of the layer at the top. However with the stratification, the positive bursts and hence skewness is suppressed, and is very close to zero all across the layer.

Figure 12 shows the kurtosis, $K \equiv \langle w^4\rangle/\langle w^2\rangle^2$, of the vertical velocity fluctuations, measured at $x/M_2 = 146$. With no stratification, the value of the kurtosis is close to the Gaussian value of 3 outside the layer. It attains high value in the layer indicating extended tails of the p.d.f. Similar behaviour was observed by Veeravalli & Warhaft (1989). With stratification the value of kurtosis becomes close to the Gaussian value of 3 throughout the layer, once again quantifying the suppressed intermittency.

3.3. *The thermal field*

3.3.1. *The temperature variance*

Figure 13 shows the vertical profile of the temperature variance, $\langle\theta^2\rangle$, normalized by the maximum value of $\langle\theta^2\rangle$ in the layer, plotted as a function of z/l_θ, where l_θ is half the width of the $\langle\theta^2\rangle$ profile, determined where $\langle\theta^2\rangle$ is half its maximum value. The

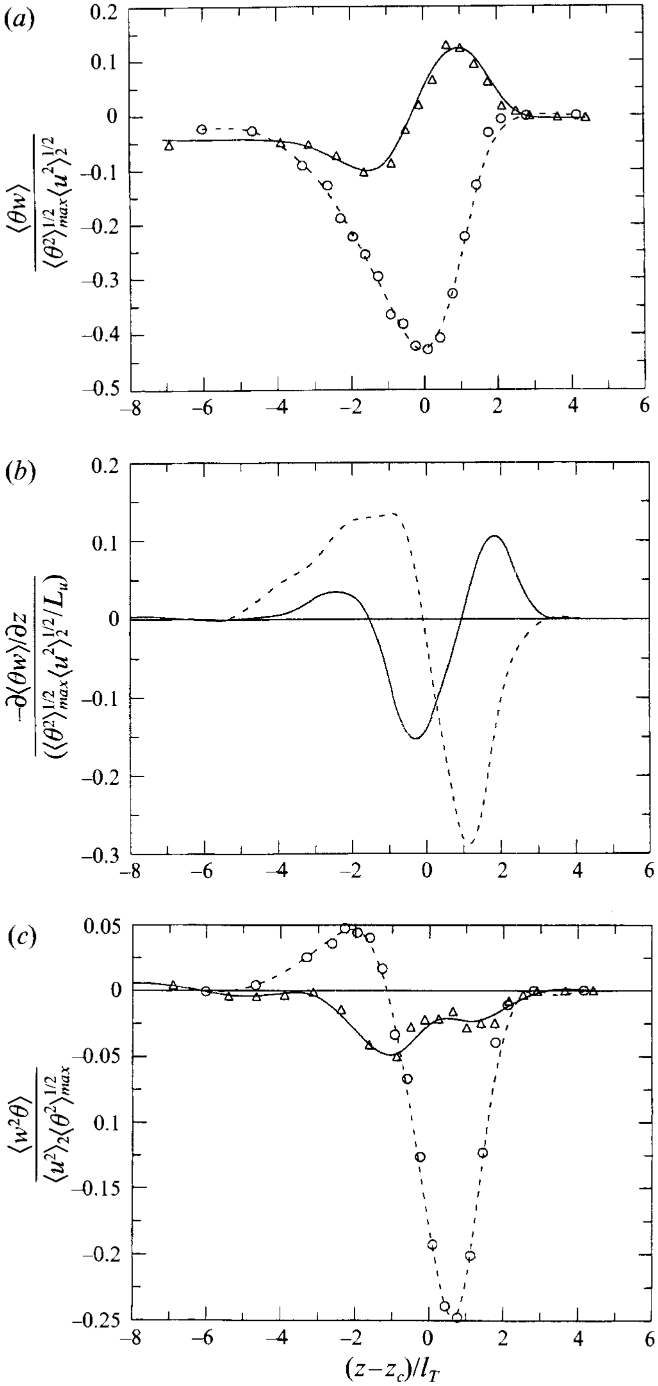

FIGURE 16. The normalized heat flux profiles $\langle\theta w\rangle/(\langle\theta^2\rangle^{1/2}_{max}\langle u^2\rangle^{1/2}_2)$, their vertical derivative, $(-\partial\langle\theta w\rangle/\partial z)/(\langle\theta^2\rangle^{1/2}_{max}\langle u^2\rangle^{1/2}_2/L_u)$, and their flux $\langle w^2\theta\rangle/(\langle u^2\rangle_2\langle\theta^2\rangle^{1/2}_{max})$ at two downstream locations; $x/M_2 = 32$ (passive) and $x/M_2 = 146$ (strongly stable). (*a*) $\langle\theta w\rangle/(\langle\theta^2\rangle^{1/2}_{max}\langle u^2\rangle^{1/2}_2)$: ○, $x/M_2 = 32$ ($Ri_B = 0.8$); △, $x/M_2 = 146$ ($Ri_B = 63$). (*b*) $-(\partial\langle\theta w\rangle/\partial z)/(\langle\theta^2\rangle^{1/2}_{max}\langle u^2\rangle^{1/2}_2/L_u)$ at $x/M_2 = 32$ (dashed line) and $x/M_2 = 146$ (solid line). (*c*) $\langle w^2\theta\rangle/(\langle u^2\rangle_2\langle\theta^2\rangle^{1/2}_{max})$: ○, $x/M_2 = 32$; △, $x/M_2 = 146$. z_c is the height where the mean temperature is $T_{min} + (T_{max} + T_{min})/2$. Other symbols have been previously defined.

collapse is quite good, as it was in the case of the thermal mixing layer of Jayesh *et al.* (1991); but comparing the collapse with a best fit Gaussian (solid line in figure 13) it is clear that the profile is asymmetric, with more spread on the strong turbulence side. In §3.1 we showed that the asymmetry in the mean temperature profile is not apparent, there the collapse (figure 4) was quite close to an error function. As for the mean profile, we have determined the evolution of the variance profile asymmetry from the half widths on the two sides of the peak of the variance profile and these are shown in figure 14. We define $l_{\theta 1}$ as the distance between the location of the peak to the point where the variance reaches half its peak value on the weak turbulence side, and $l_{\theta 2}$ as the distance between the location of the peak to the point where the variance reaches half its peak value on the strong turbulence side. Figure 14 shows $l_{\theta 1}/M_2$, $l_{\theta 2}/M_2$ and $l_{\theta 1}/l_{\theta 2}$ plotted against the bulk Richardson number. Qualitatively the behaviour of half widths of the variance profile is very similar to that of the mean temperature profile (figure 6). Like L_{T2}, $l_{\theta 2}$ (the large-scale side) accounts for most of the thickening and thinning of the profile, and once again we note that as the stratification effect becomes stronger the asymmetry becomes less prominent and the ratio, $l_{\theta 1}/l_{\theta 2}$, seems to be approaching unity.

Figure 15 shows $\langle\theta^2\rangle^{1/2}_{max}/\Delta T$ and l_T/l_θ plotted as a function of the bulk Richardson number. The quantity $\langle\theta^2\rangle^{1/2}_{max}/\Delta T$ (lower points) shows a slight decrease with increasing Ri_B. A decrease in this quantity was also observed by Jayesh *et al.* (1991, figure 11) in their thermal mixing layer. In a passive thermal mixing layer in homogeneous turbulence, this quantity is constant (Ma & Warhaft 1986). Here, as in Jayesh *et al.* (1991) the buoyancy depletes the temperature variance resulting in the decrease in $\langle\theta^2\rangle^{1/2}_{max}/\Delta T$. The trend of l_T/l_θ (figure 15, upper points) shows that for small values of Ri_B, the scalar variance width increases faster than the mean temperature width, but this is reversed for higher values of Ri_B. We note from (1) that the gradient of the heat flux determines the rate of thickening (or thinning) of the mean profile whereas (3) suggests that it is mainly the transport term, $-\partial(\langle\theta^2 w\rangle/2)/\partial z$, which determines the rate of thickening (or thinning) of the variance profile. (The production (or sink, as the case may be) and dissipation terms in the scalar variance equation mainly determine the value of variance as opposed to the spread of the variance profile.) The trend in l_T/l_θ suggests that for moderate stratification ($Ri_B < 10$) the triple moment transport causes l_θ to increase at a greater rate than l_T. However, for the very strong stratification ($Ri_B \sim 80$), when the heat flux has collapsed (see below) these two quantities become equal. (Note that for the neutral part of the flow near the grid ($Ri_B \sim 0.1$), l_T/l_θ is also close to unity.)

3.3.2. *Transport and production terms*

In §3.1 (figure 6) we discussed the evolution of the mean temperature profile and showed that initially the layer thickens (until $Ri_B \sim 4$) and then it thins as the Ri_B increases further. We now examine the terms in the second-order equations to elucidate the dynamics within the layer. Figure 16(*a*) shows the flux at two downstream locations; $x/M_2 = 32$ ($Ri_B = 0.8$) where stratification is insignificant and the flux is down the gradient (negative $\langle\theta w\rangle$), and in the stably stratified region further downstream ($x/M_2 = 146$, $Ri_B = 63$) where the flux has reversed sign in the weak turbulence region above the centreline of the layer and has become counter-gradient. Countergradient heat flux has been observed both in numerical simulations (Schumann 1987; Riley, Metcalfe & Weissmann 1981) and in water-tunnel and wind-tunnel experiments (Yoon & Warhaft 1990; Stillinger *et al.* 1983). Various mechanisms have been suggested for its observed behaviour: the exchange between the potential energy and kinetic energy (Yoon & Warhaft 1990); the dissipation of temperature fluctuations being too small to balance production (Schumann 1987); the vertical turbulent transport of scalar variance (Finger & Schmidt 1986; Deardorff 1986); wavelike motions (Komori & Ueda 1983), and buoyancy–turbulence interactions which couple energy flux to the gradients of the vertical heat flux and temperature variance (Zeman & Lumley 1976). A general description of interpretation of the heat flux measurements in stable stratification is to be found in Hunt (1985). Of course not all of the above mentioned mechanisms are independent. We shall make use of some of these concepts to explain the behaviour of the buoyancy and transport terms in the mean temperature, scalar variance and kinetic energy equation.

The vertical divergence of the heat flux, $-\partial\langle\theta w\rangle/\partial z$ which appears in the mean temperature evolution equation (equation (1)), is plotted in figure 16(*b*). Close to the grid it is negative above the layer and positive below, crossing the zero line at the centre. Equation (1) then implies thickening of the layer. Far downstream there is a region below the centreline where $-\partial\langle\theta w\rangle/\partial z$ is negative, and a region above the centreline where $-\partial\langle\theta w\rangle/\partial z$ is positive. Here cooler air is now moving towards the cooler (lower) region and warmer air is moving towards warmer (upper) region of the mixing layer. This results in a steepening of the mean profile since the action of the flux is opposite to the eroding (thickening) action that occurs in the neutral (upstream) situation. Thus the mean half width is reduced and the layer thins. This is also discussed in §1 in terms of (1). A similar result was observed by Jayesh *et al.* (1991) in their thermal mixing layer (figure 16 in that paper). Figure 16(*c*) shows $\langle w^2\theta\rangle$ for the two downstream locations, $x/M_2 = 32$ and 146. The gradient of this quantity is the transport term in the scalar flux equation (equation (4)). Close to the grid $\langle w^2\theta\rangle$ is positive below the centre and negative above, indicating that (the modulus of) the flux is carried away from the centre to the edges. Far downstream $\langle w^2\theta\rangle$ is negative across the whole layer, i.e. the flux of $\langle\theta w\rangle$ is downwards. Note that here the ratio of $\langle w^2\theta\rangle$ to its value upstream is very small (~ 0.1, figure 16*c*), whereas the flux (magnitude) itself is still relatively large; it has only decreased by a factor of four from its upstream value (figure 16*a*).

Figure 17(*a*) shows the vertical flux of turbulent kinetic energy $\langle kw\rangle$, where $k \equiv \frac{1}{2}(u^2+v^2+w^2)$, again at $x/M_2 = 32$ (weak stratification) and at $x/M_2 = 146$ where the stratification has become pronounced. Figures 17(*b*) and 17(*c*) show the vertical derivative of $\langle kw\rangle$ at these locations and compare them with the buoyancy term, $(g/T_0)\langle\theta w\rangle$ (equation (2)). At $x/M_2 = 32$, $\langle kw\rangle$ is positive throughout the layer (figure 17*a*). Thus turbulent kinetic energy is transported from the high kinetic energy region below the inflexion point (in figure 17(*b*) $-\partial\langle kw\rangle/\partial z$ is negative in this region), to the low kinetic energy region above the inflexion point ($-\partial\langle kw\rangle/\partial z$, positive). The buoyancy term is a sink of kinetic energy ($(g/T_0)\langle\theta w\rangle$ is negative) throughout the layer at this location (figure 17*b*). Thus kinetic energy is being transferred to the potential energy. However at $x/M_2 = 146$ (figure 17*c*) $(g/T_0)\langle\theta w\rangle$ is a source term above the inflexion point. Here the kinetic energy is increasing at the expense of potential energy. The cold fluid particles (or hot fluid particles) thrown up (or down) by the mechanical energy gain potential energy, and if the diffusion process is not fast enough, i.e. if the small-scale gradients experienced by the fluid particle in question are not steep enough, then the fluid particle is essentially in an unstable equilibrium and tends to go back to a location where it is in stable equilibrium; this causes restratification and the buoyancy term becomes a source term. Although $(g/T_0)\langle\theta w\rangle$ changes sign at the

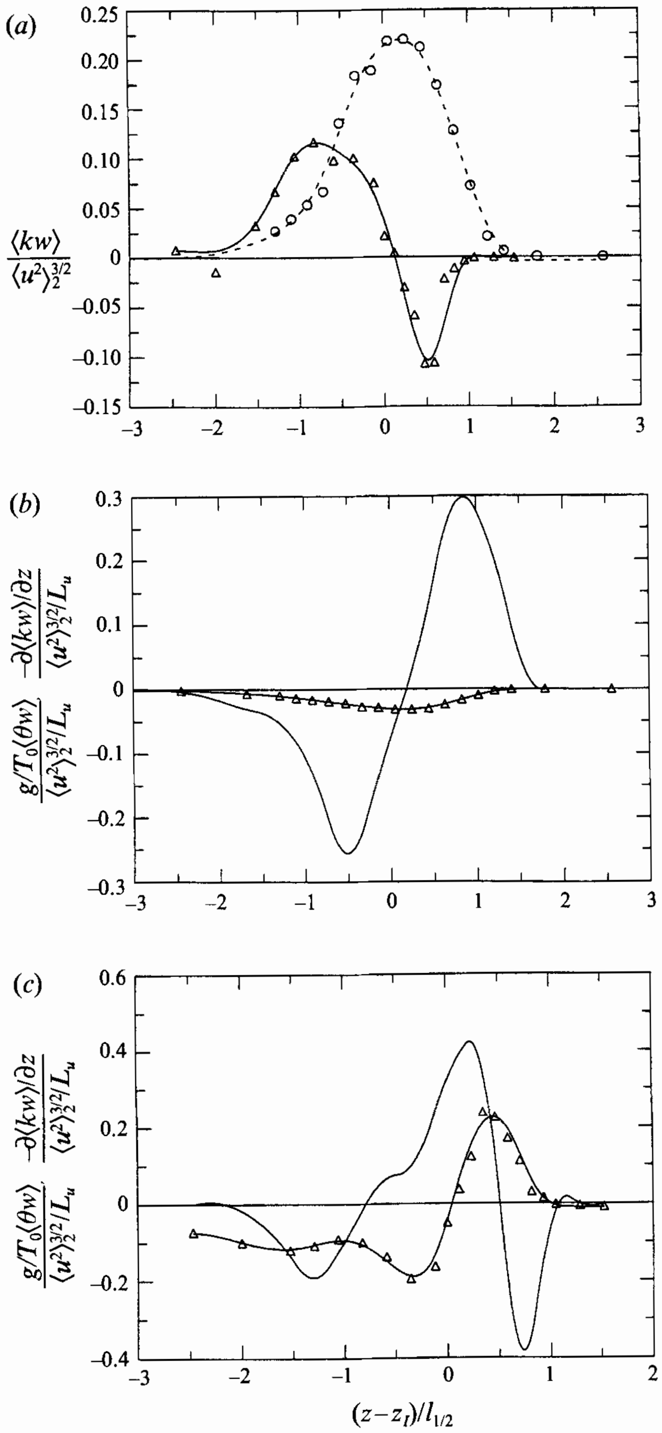

FIGURE 17. The normalized vertical flux of kinetic energy, $\langle kw \rangle / \langle u^2 \rangle_2^{3/2}$, kinetic energy production (or destruction), $(g/T_0)\langle \theta w \rangle / (\langle u^2 \rangle_2^{3/2}/L_u)$ and transport $-\partial \langle kw \rangle / \partial z / (\langle u^2 \rangle_2^{3/2}/L_u)$ at two downstream locations, $x/M_2 = 32$ (passive) and $x/M_2 = 146$ (strongly stable). (a) $\langle kw \rangle / \langle u^2 \rangle_2^{3/2}$: ○, $x/M_2 = 32$; △, $x/M_2 = 146$. (b) △, $(g/T_0)\langle kw \rangle / (\langle u^2 \rangle_2^{3/2}/L_u$; solid line, $-\partial \langle kw \rangle / \partial z / (\langle \partial u^2 \rangle_2^{3/2}/L_u)$ at $x/M_2 = 32$. (c) Same as (b) but at $x/M_2 = 146$. z_I is the inflexion height of the $\langle u^2 \rangle$ profile.

inflexion point, $-\partial\langle kw\rangle/\partial z$ changes sign higher up in the weak turbulence region (figure 17*c*). Thus there is a small region in which there is a countergradient heat flux but the kinetic energy is still transported down the gradient. Higher up, as the countergradient heat flux reaches its maximum, the kinetic energy also becomes counter gradient.

Figure 18(*a*) shows the vertical flux of temperature variance, $\langle\theta^2 w\rangle$, plotted against z/l_θ at $x/M_2 = 32$ and 146, and figures 18(*b*) and 18(*c*) show the vertical derivatives of $\langle\theta^2 w\rangle$ and compare these derivatives with the temperature variance production term, $-\langle\theta w\rangle\,\partial T/\partial z$ (equation (3)). For the passive location ($x/M_2 = 32$), $\langle\theta^2 w\rangle$, is positive above the location where $\langle\theta^2\rangle$ is maximum and negative below, indicating that the scalar variance is carried away from its peak towards the edges of the layer ($-\partial(\frac{1}{2}\langle\theta^2 w\rangle)/\partial z$ is negative in the centre and positive at the edges in figure 18(*b*)). However at $x/M_2 = 146$ ($Ri_B = 63$), the sign of $\langle\theta^2 w\rangle$ is opposite to that at $x/M_2 = 32$ ($Ri_B = 0.8$). Here the transport of scalar variance is towards the centre of the layer. This is evident from figure 18(*c*). Here the transport term, $-\partial(\frac{1}{2}\langle\theta^2 w\rangle)/\partial z$, is positive near the peak of the scalar variance. (A similar change of sign of $\langle\theta^2 w\rangle$ was observed by Jayesh *et al.* 1991.) The production of scalar variance, $\langle\theta w\rangle\,\partial T/\partial z$ (figure 18*b*, *c*), is positive throughout the layer at $x/M_2 = 32$ (figure 18*b*). At $x/M_2 = 146$ (figure 18*c*) however, the production term is negative for a significant portion of the layer, including the location of the peak of the scalar variance.

We have only reported here the production and transport terms for the turbulent kinetic energy, heat flux and temperature variance and thus the complex inter dependence of the second-order equations (equations (1)–(4)) is far from being fully understood for this flow. However, our results (figures 16–18) clearly show that when the flux reverses sign in the upper part of the layer, there is a production of turbulent kinetic energy (the buoyancy term acts as a source in equation (2)) and a destruction of temperature variance owing to the change in sign of the production term, $-\langle\theta w\rangle\,\partial T/\partial z$, of that quantity (equation (3)). Since the heat flux has changed sign, this is to be expected. Perhaps less obvious is the role of the transport terms. Figure 17(*c*) shows that the vertical divergence of the flux of kinetic energy remains relatively unaffected until very high up in the layer, not changing sign until well beyond the inflexion point in the kinetic energy variance profile. On the other hand, the divergence of the vertical flux of temperature variance changes sign throughout most of the layer when the stratification becomes strong (figure 18*c*). Noting that the sign of the heat flux changes, it can be inferred from figure 16(*c*) that the stratification affects the vertical divergence of the heat flux transport across the whole of the layer. Thus for this flow, the kinetic energy transport is less severely affected by the stratification than the temperature variance or heat flux transport. This is consistent with our earlier observation that the ratio of the thermal to velocity lengthscale decreases as the stratification becomes stronger (figure 7). Finally, in our description of the graphs of figures 16–18 we have neglected to comment on some of the less salient features such as the sign reversal of the flux divergence terms at the very edges of the layer. It should be noted that for $|(z-z_{max})/l_\theta| \gtrsim 2$, the temperature (and velocity) variance becomes very small, particularly on the low turbulence side of the layer (figure 13) and thus derivatives of the triple moment quantities involving θ at the edge of the layer are likely to suffer inaccuracy.

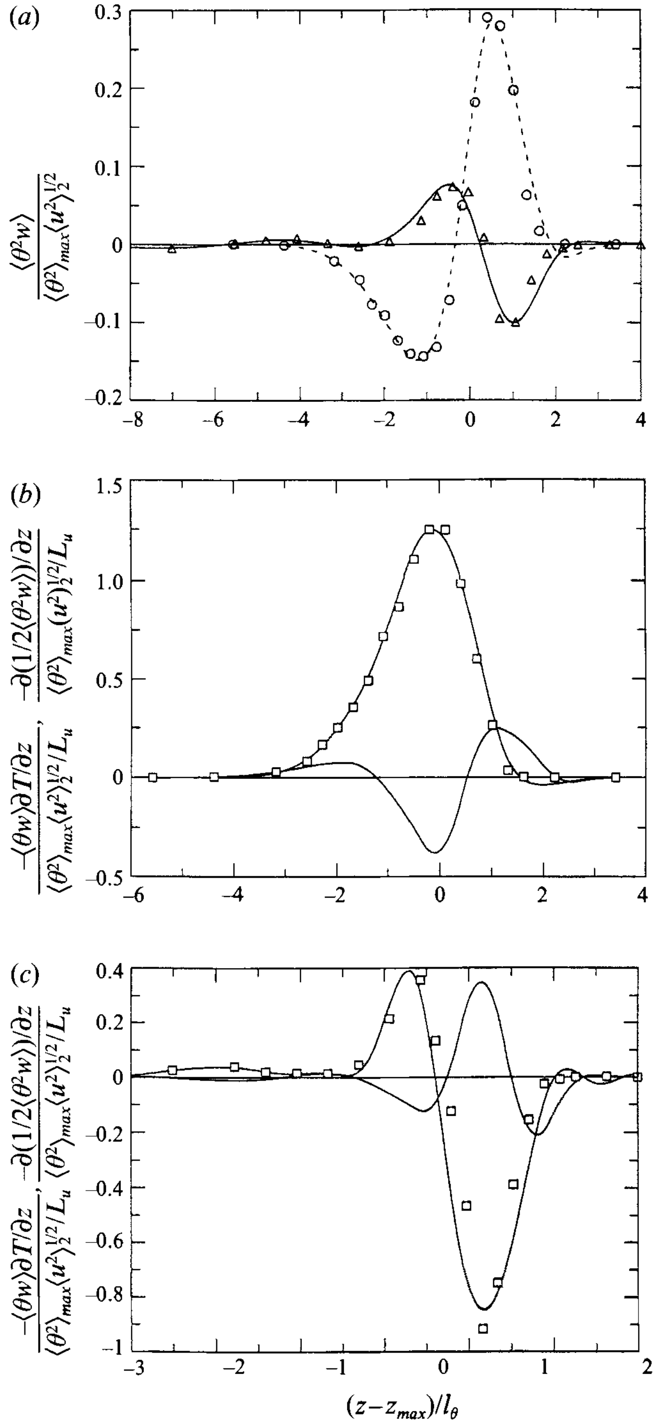

FIGURE 18. Vertical profiles of the normalized flux of temperature variance, $\langle\theta^2 w\rangle/(\langle\theta^2\rangle_{max}\langle u^2\rangle_2^{1/2})$, the production of temperature variance, $-\langle\theta w\rangle\,\partial T/\partial z/(\langle\theta^2\rangle_{max}\langle u^2\rangle_2^{1/2}/L_u)$, and the transport of temperature variance $-\partial(\frac{1}{2}\langle\theta^2 w\rangle)/\partial z/(\langle\theta^2\rangle_{max}\langle u^2\rangle_2^{1/2}/L_u)$, at two downstream locations, $x/M_2 = 32$ and 146. (*a*) $\langle\theta^2 w\rangle/(\langle\theta^2\rangle_{max}\langle u^2\rangle_2^{1/2})$: ○, $x/M_2 = 32$ and △, $x/M_2 = 146$. (*b*) □, $-\langle\theta w\rangle\,\partial T/\partial z/(\langle\theta^2\rangle_{max}\langle u^2\rangle_2^{1/2}/L_u)$; solid line, $-\partial(\frac{1}{2}\langle\theta^2 w\rangle)/\partial z/(\langle\theta^2\rangle_{max}\langle u^2\rangle_2^{1/2}/L_u)$ at $x/M_2 = 32$. (*c*) The same as (*b*) but at $x/M_2 = 146$. z_{max} is the height at which $\langle\theta^2\rangle$ is maximum.

3.3.3. *Conditional heat flux*

In order to further understand the effects of buoyancy we determined the conditional heat flux ξ', i.e. heat flux conditioned on its particular value of temperature, defined as (e.g. Ross 1988)

$$\xi' \equiv \langle w\theta \mid \theta \rangle. \tag{8}$$

This statistic, as will be shown, has well-defined properties for the passive case and shows the effects of buoyancy in a very lucid manner. Let us first consider the case of a passive linear temperature profile in isotropic grid turbulence and assume† a joint normal distribution of w and θ, i.e.

$$f(w,\theta) = \frac{1}{2\pi\sigma_\theta\sigma_w(1-\rho^2)^{1/2}}\exp\left\{-\frac{1}{2(1-\rho^2)}\left[\left(\frac{\theta}{\sigma_\theta}\right)^2 - \frac{2\rho(\theta w)}{\sigma_\theta\sigma_w} + \left(\frac{w}{\sigma_w}\right)^2\right]\right\}, \tag{9}$$

where ρ is the correlation coefficient between the vertical velocity fluctuations, w, and the temperature fluctuations, θ. The standard deviation for w and θ are σ_w and σ_θ, respectively, and their means are by definition zero. The p.d.f. of vertical velocity conditioned on temperature, $f(w \mid \theta)$, can then be found using the relation

$$f(w \mid \theta) = \frac{f(w,\theta)}{f(\theta)}, \tag{10}$$

where $f(\theta)$ is the marginal p.d.f. of the temperature fluctuations. Using equation (10), the conditional expectation of the vertical velocity conditioned on the temperature, $\langle w \mid \theta \rangle$, can be determined by

$$\langle w \mid \theta \rangle = \int_{-\infty}^{\infty} f(w \mid \theta)\, w\, \mathrm{d}w. \tag{11}$$

This gives a linear relationship between $\langle w \mid \theta \rangle$ and the temperature fluctuations:

$$\frac{\langle w \mid \theta \rangle}{\sigma_w} = \rho\frac{\theta}{\sigma_\theta}. \tag{12}$$

In figure 19 we show measurements for a linear mean gradient of temperature in homogeneous grid-turbulence taken from the data of Yoon & Warhaft (1990) in the region close to the grid where the flow is passive. Note that the straight line shown in figure 19 is not a best fit straight line; it is the straight line given by equation (12). The measured value of the correlation coefficient has been used for ρ, and the measured value of the root mean square of the vertical velocity fluctuations, w', and temperature fluctuations, θ', has been used for σ_w and σ_θ, respectively. The fit to the data is remarkably good, verifying that for passive linear temperature profile the data is indeed joint normal. This is consistent with the results of Tavoularis & Corrsin (1981) for a passive temperature profile with shear.

---

† In fact it has been shown by Jayesh & Warhaft (1992) that for linear mean profile of a scalar, the probability density function (p.d.f.) of the scalar has non-Gaussian tails for turbulence Reynolds numbers greater than about 70; hence when the Reynolds number is large enough, the joint p.d.f. of the vertical velocity fluctuations and the temperature fluctuations cannot strictly be taken to be a joint normal. However, for the turbulence Reynolds numbers considered here we will show that the joint normal approximation does hold.

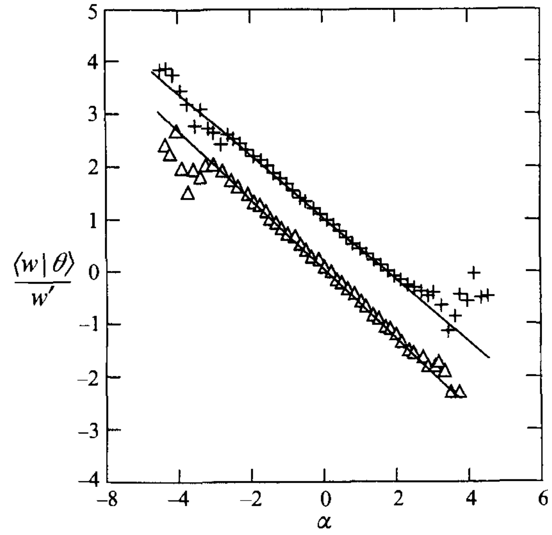

FIGURE 19. The vertical velocity fluctuations conditioned on the temperature fluctuations, $\langle w|\theta\rangle$, normalized by the r.m.s. velocity fluctuation w', as a function of $\alpha \equiv \theta/\sigma_\theta$. Here θ is the instantaneous temperature and σ_θ is its r.m.s. value. This is for the passive data of Yoon & Warhaft (1990). The temperature profile is linear and the flow is conventional (homogeneous) grid turbulence. $U = 2.8\ \mathrm{m\,s^{-1}}$, $\partial T/\partial z = 55\ ^\circ\mathrm{C\,m^{-1}}$. △, $x/M = 36.5$, $\rho = -0.67$; +, $x/M = 76.5$, $\rho = -0.60$. The $x/M = 76.5$ data is shifted up by one non-dimensional unit. The solid line is equation (12).

The expression for conditional heat flux is given by

$$\begin{aligned}\langle w\theta|\theta\rangle &= \int_{-\infty}^{\infty} \theta w f(w|\theta)\,\mathrm{d}w\\ &= \theta\int_{-\infty}^{\infty} w f(w|\theta)\,\mathrm{d}w\\ &= \theta\langle w|\theta\rangle. \qquad (13)\end{aligned}$$

Substituting the expression for $\langle w|\theta\rangle$ from (13) into (14) we find

$$\langle w\theta|\theta\rangle = \rho\frac{\sigma_w}{\sigma_\theta}\theta^2. \qquad (14)$$

Defining the normalized conditional heat flux and the normalized temperature as

$$\xi = \frac{\langle w\theta|\theta\rangle}{|\langle w\theta\rangle|}, \qquad (15)$$

$$\alpha = \frac{\theta}{\sigma_\theta}, \qquad (16)$$

equation (14) may be rewritten as

$$\xi = -\alpha^2, \qquad (17)$$

which is an inverted parabola. Figure 20 shows this statistic calculated for the same passive data as figure 19. It is evident in figure 20 that the data follows the inverted parabola (solid line) closely.

For a buoyant scalar, however, the data show deviation from the parabola. Figure 21 shows the conditional heat flux extracted from the measurements done by Yoon &

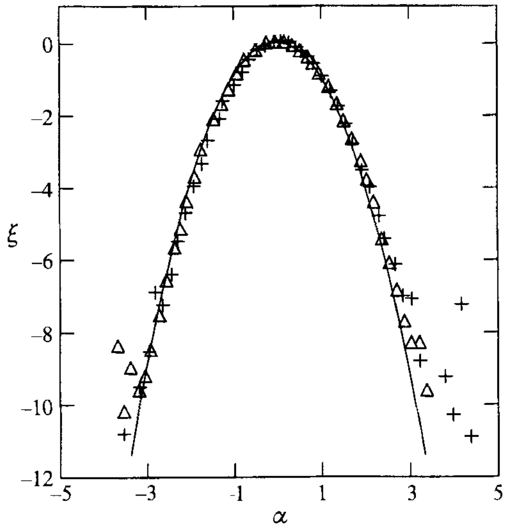

FIGURE 20. The normalized conditional heat flux, $\xi \equiv \langle w\theta | \theta \rangle / |\langle w\theta \rangle|$ plotted as a function of $\alpha \equiv \theta/\sigma_\theta$ for the same passive data as figure 19. The solid line (parabola) is equation (17).

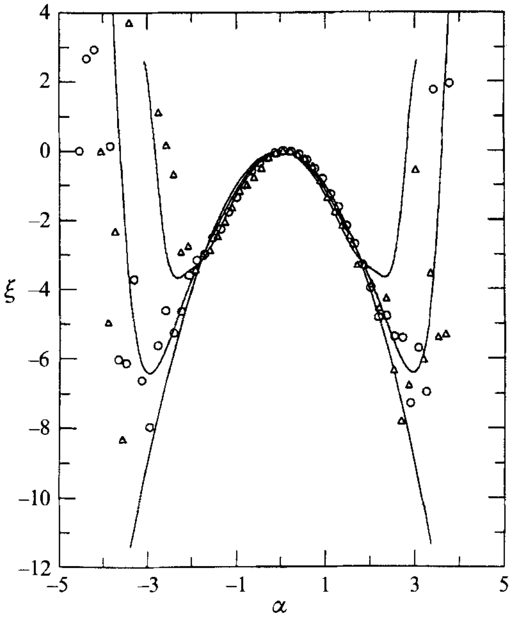

FIGURE 21. ξ *vs.* α for data of Yoon & Warhaft (1990) where the flow is strongly stable. ○, $U = 2.8$ m s^{-1}, $\partial T/\partial z = 55$ °C, $x/M = 116.5$, $\rho = -0.39$; □, $U = 3.6$ m s^{-1}, $\partial T/\partial z = 50$ °C, $x/M = 196.5$, $\rho = -0.16$. The value of ξ for the passive case is the inverted parabola. A symmetric smooth curve has been drawn along the data points.

Warhaft (1990) far downstream where the linear temperature profile now causes pronounced stable stratification. Close to $\theta = 0$, the data still follows the parabola but for temperatures far away from the mean, ξ curls up. Fluid particles with temperatures distant from the mean are far away from the equilibrium, and the restoring buoyancy force is large enough to affect the direction of the vertical velocity of the particle, leading to curling up of the ξ profile. Note that for a large enough temperature deficit

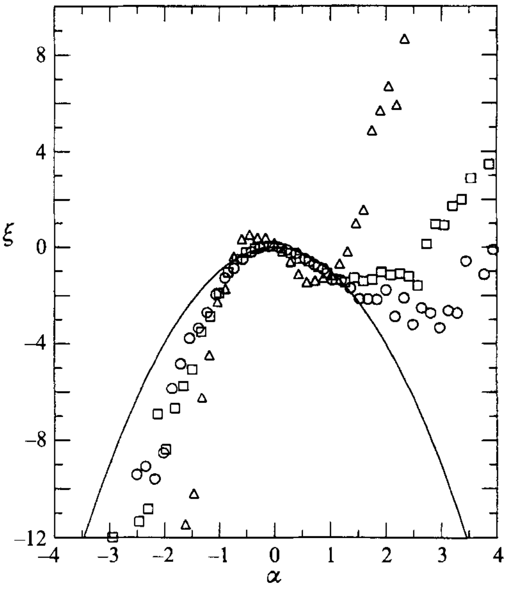

FIGURE 22. The normalized conditional heat flux ξ as a function of α for the present experiment. The data is at $x/M_2 = 146$ in the strongly stable region. ○, $z/M_2 = 12.04$; □, $z/M_2 = 12.67$; △, $z/M_2 = 13.0$. ——, the passive case (equation (17)).

(or surplus) countergradient of the heat flux is observed (positive ξ). Figure 21 clearly shows that, in the mean sense, the intense fluctuations are affected by the buoyancy, whereas the weaker fluctuations are still behaving as though they were a passive scalar. This result is consistent with the recent experiment of Thoroddsen & Van Atta (1992), also done for linearly stratified grid generated turbulence. They find that the assumption of joint normality provides a good estimate of the p.d.f. of the instantaneous heat flux itself, except for in the tails of the distribution, where there is some departure. Only one p.d.f. is reported in their work and it is close to the grid where buoyancy forces are comparatively small. We expect that measurements of this quantity further downstream would show a greater departure from the joint-normal assumption, as do ours.

Now we turn our attention to the conditional heat flux for the present flow. Figure 22 shows the normalized conditional heat flux for three vertical locations ($z/M_2 = 12.04$, $z/M_2 = 12.67$, $z/M_2 = 13.0$) in the stably stratified layer, measured at $x/M_2 = 146$. The inflexion point at this location is at $z/M_2 = 13.0$, thus measurements shown are from the region just below it ($\sim 1 M_2$), to the inflexion point itself. Clearly the data do not follow an inverted parabola and thus w and θ are not joint normal. This is to be expected since the turbulent velocity field and the temperture profile are inhomogeneous (figures 4 and 5). For temperature fluctuations less than the local mean, the conditional heat flux still decreases, but faster than the parabolic form of figure 20. This may be explained in terms of the inhomogeneity of the mean temperature profile which leads to an asymmetric p.d.f. for temperature fluctuations, with a longer tail on the positive side. (The asymmetry will depend on the location in the layer, and for the cases shown in figure 22 the longer positive tail is the case.) Since we have normalized the abscissa by θ' which is the r.m.s. of the overall p.d.f., the data must fall more sharply than the parabola given by equation (18), for negative values of α. However for θ/θ' positive, as the stratification becomes more pronounced, ξ begins to increase with θ/θ' and becomes positive for the two most stable positions shown in figure 22, indicating that for large θ/θ' there is a counter-gradient heat flux. The way our flow is set up, positive temperature (in terms of departure from the local mean) comes from the weak turbulence above and negative temperature comes from the strong turbulence below. Thus, figure 22 shows that the buoyancy is acting most strongly on the low-energy turbulence, as would be expected. However, the plot provides quantitative relationship between the stratification and the intensity of the fluctuations, and indicates that for positive θ/θ', its effects are small unless the fluctuations exceed approximately one r.m.s. (it will be shown below that for a passive case the maximum contribution to the heat flux is from $\theta = \surd 2\theta'$). Note for the strongest stratification, the dramatic increase of $\langle \theta w \mid \theta \rangle$ with θ.

It is not evident from figure 22 whether the contribution from the large temperature fluctuations to the total flux is significant or not; to determine this we define

$$\begin{aligned} W'(\theta) &\equiv \text{contribution to the total heat flux from a given temperature } \theta \\ &= \langle w\theta \mid \theta \rangle f(\theta). \end{aligned} \tag{18}$$

First we will determine the form of this quantity for the passive linear profile case. Substituting the expressions for $\langle w\theta \mid \theta \rangle$ from (14), and for the marginal p.d.f. of temperature, $f(\theta)$, from our joint normal assumption, we find

$$W'(\theta) = \rho \frac{\sigma_w}{\sigma_\theta} \theta^2 \frac{1}{(2\pi)^{1/2} \sigma_\theta} \exp\left(-\frac{\theta^2}{2\sigma_\theta^2} \right). \tag{19}$$

If we define

$$W = \frac{W'}{\sigma_w}, \tag{20}$$

then we have from (19)

$$W = \rho \alpha^2 \frac{1}{(2\pi)^{1/2}} \exp\left(-\tfrac{1}{2}\alpha^2\right). \tag{21}$$

An interesting feature to note here is that for a joint normal distribution of w and θ (e.g. passive linear mean temperature gradient in homogeneous turbulence (Yoon & Warhaft (1990), close to the grid)) the peak of W occurs at $\alpha = \surd 2$, i.e. the maximum contribution comes from $\theta = \surd 2\theta'$. We have plotted W in figure 23. The solid line shows (21) with $\rho = -0.65$, which is a typical value for passive temperature fluctuations. The area under the curve is the total heat flux. The other three cases shown in figure 23 are for the same data as figure 22 and their area is diminished owing to the stratification. All the stratified cases shown are asymmetric with a smaller contribution from the $\theta > 0$ region. This is to be expected because the turbulence intensity at the top of the layer is smaller. The peak value of the contribution to heat flux is smaller than the passive value of $\rho\surd 2/(\mathrm{e}\surd\pi)$, and the peak has shifted towards smaller $|\theta|$. Note that while most of the contribution to the countergradient heat flux is for $\theta > 0$, there appears to be a small contribution from $\theta < 0$. The maximum contribution to the countergradient heat flux ($W > 0$) occurs at a larger $|\theta|$ for $\theta > 0$ than for $\theta < 0$. This is so because for the countergradient heat flux to occur, $\theta > 0$ must be associated with $W > 0$, i.e. the fluid particle must be coming from below for $\theta > 0$ and vice versa for $\theta < 0$. Thus for $\theta > 0$ the maximum countergradient heat flux would correspond to the fluctuations being affected most in the strong turbulence region, which is expected to be at a higher value of θ than for the weak turbulence. Figure 23 also shows the values of temperature for which the flux is suppressed most, and the values of temperature for which a significant counter-gradient heat flux occurs

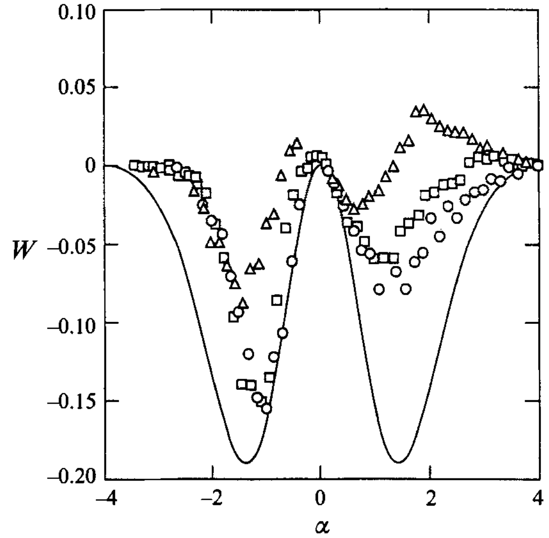

FIGURE 23. The normalized contribution to the heat flux from a given temperature, $\langle w\theta \mid \theta \rangle f(\theta)$, where $f(\theta)$ is the marginal p.d.f. of temperature plotted as a function of α. Same positions and symbols as for figure 22. The solid line is for the passive case, equation (21).

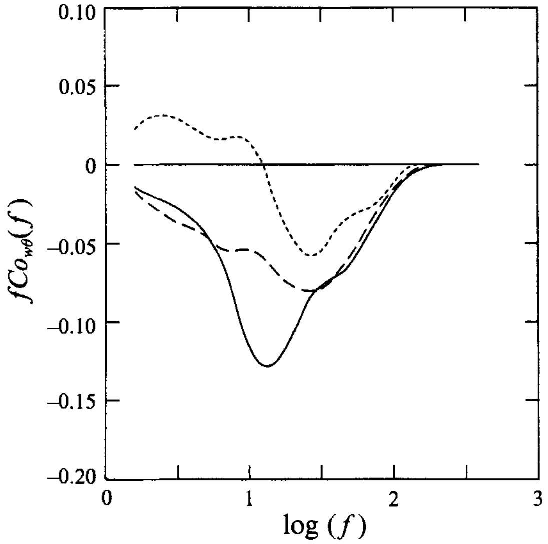

FIGURE 24. The co-spectrum of w and θ multiplied by the frequency, f, at the same locations as the figures 22 and 23. Solid line, $z/M_2 = 12.04$; long dashes, $z/M_2 = 12.67$; short dashes, $z/M_2 = 13.0$.

(positive W). For instance, although in figure 22 two locations were showing countergradient heat flux, figure 23 shows that only for the most stable case is there a significant contribution from the countergradient heat flux.

Cospectra for the same three locations of figure 22 are shown in figure 24. What figure 22 shows in temperature space, figure 24 shows in frequency (or wavenumber) space. The short-dashed curve in figure 24 shows counter-gradient heat flux at low wave number. Thus the conditional heat flux plots (figures 22 and 23) in conjunction with the co-spectra (figure 24) show that the counter-gradient heat flux arises from the intense bursts of instantaneous temperature fluctuations occurring at the large scales.

However, the conclusion that the weak turbulence is preferentially affected by buoyancy cannot be directly seen in the cospectra (figure 24). Further the second curve in figure 22 is already showing signs of counter-gradient heat flux, whereas this effect is completely masked in figure 24. This is essentially due to the fact that the conditional heat flux and the cospectra are two different kinds of averaging, one is for a given temperature and the other is for a given frequency (or wavenumber), and it turns out that one averaging is more sensitive to the buoyancy effects than the other.

4. Summary and conclusions

Our experiment has shown that stable stratification radically alters the dynamics and transport characteristics of the shearless turbulence mixing layer, previously investigated for the passive case by Veeravalli & Warhaft (1989, 1990). The stratification completely destroys the intermittent penetration of the large-scale intense turbulence below the layer that is the principal agent of mixing for the passive case. Instead of spreading, the layer thins with downstream distance or increasing Richardson number (figures 6 and 14), a finding in common with grid-stirred tank experiments (Fernando 1992), where the density gradient becomes sharper at high Richardson numbers. Both the skewness and kurtosis of the vertical velocity fluctuations, which are very large in the passive case, are reduced to the Gaussian values of 0 and 3, respectively (figures 8–12). The stratification causes a countergradient heat flux in the upper part of the layer (figure 16), and also a region of countergradient flux of kinetic energy (figure 17). The countergradient heat flux results in a depletion of the temperature variance, the fluctuating potential energy being converted into kinetic energy. Thus the production terms of kinetic energy and temperature variance (equations (2) and (3)) change sign (figures 17 and 18). We have also shown that the triple moment transport terms change sign in the upper part of the layer. Hence temperature variance is transported to the centre of the layer (where it has a peak value) rather than away from it (figure 18). The situation is similar for the triple moment transport of vertical kinetic energy (figure 17) and heat flux (figure 16).

We have examined the details of the heat flux by determining its value conditioned on the value of the simultaneous temperature fluctuations (figures 22 and 23). We show that the stratification first affects the largest temperature fluctuations and as it becomes stronger the weaker ones are affected. The countergradient heat flux is associated with large temperature fluctuations which have values greater than one standard deviation (figure 22), with the maximum contribution arising from fluctuations even larger than this (figure 23). By means of $w\theta$ cospectra (figure 24) we have shown that the countergradient heat flux occurs at low frequencies (or large wavelengths). Thus we can infer that the large temperature fluctuations affected by stratification (figures 22 and 23) are associated with large scales. We have shown that there is a strong departure from the often made assumption of joint normality between the velocity and temperature fluctuations when there is stratification (figures 21 and 22). However, for passive temperature fluctuations (with linear temperature profile, and for low enough Reynolds numbers), we show that the assumption of joint normality is extremely sound (figures 19 and 20), in keeping with the previous findings of Tavoularis & Corrsin (1981) for a passive temperature profile in a shear flow.

Our results have much in common with our previous study of a stratified layer in a conventional grid turbulence (Jayesh *et al.* 1991). There also we found that the heat flux collapsed. This resulted in a small but significant depletion of the vertical velocity variance within the layer, and this was reflected in the flow visualization. However, because the flow was close to homogeneous, there was relatively little large-scale intermittency observed in the velocity field. Here, on the other hand, the velocity field above the layer was deliberately suppressed by means of the grid construction. Thus intermittency was *a priori* a principal method of transport for the passive case (the other mode being turbulent diffusion, Veeravalli & Warhaft 1989). For this configuration our experiment has clearly shown that the stratification completely suppresses the large-scale intermittency and that transport is only by turbulent diffusion, be it up or down the gradient.

We thank Mr Ed Jordan for his technical help in all aspects of the experiment and Ms Nicole Trotter for constructing and performing the initial testing of the composite grid. This work was supported by the US Department of Energy, Basic Energy Sciences (Contract no. DE-FG02-88ER13929) whom we also thank.

Jayesh died in a swimming accident while this paper was in press. He was 28. The work reported here is part of his PhD thesis which was completed in January, 1994. His bold and open-minded approach is deeply missed.

REFERENCES

ALEKSENKO, N. V., BUKREEV, V. I. & KOSTOMAKHA, V. A. 1985 Interaction of two isotropic turbulent fields without shear. *Zh. Prikl. Mekh. Tekh. Fiz.* **1**, 57–62.

ANDRÉ, J. C., DEMOOR, F., LACERURE, P., THERRY, G. & DUVACHAT, R. 1978 Modeling the 24-hour evolution of the mean and turbulent structures of the planetary boundary layer. *J. Atmos. Sci.* **35**, 1861–1883.

BRITTER, R. E., HUNT, J. C. R., MARSH, G. L. & SNYDER, W. H. 1983 The effect of stable stratification on turbulent diffusion and decay of grid turbulence. *J. Fluid Mech.* **127**, 27–44.

BROWAND, F. K. & HOPFINGER, E. J. 1985 The inhibition of vertical turbulent scale by stable stratification. In *Turbulence and Diffusion in Stable Environments* (ed. J. C. R. Hunt), pp. 15–27. Oxford University Press.

CAUGHEY, S. J. 1982 Observed characteristics of the atmospheric boundary layer. In *Atmospheric Turbulence and Air Pollution Modelling* (ed. F. T. M. Nieuwstadt & H. van Dop), pp. 107–158. Reidel.

CHAMPAGNE, F. H. & SLEICHER, C. A. 1967 Turbulence measurement with inclined hot wire. Part 2. *J. Fluid Mech.* **28**, 177–182 (and Corrigendum **31**, 1968, 416).

CRAPPER, P. F. & LINDEN, P. F. 1974 The structure of turbulent density interfaces. *J. Fluid Mech.* **65**, 45–63.

DEARDORFF, J. W. 1966 The counter-gradient heat flux in the lower atmosphere and in the laboratory. *J. Atmos. Sci.* **23**, 503–506.

DICKEY, T. D. & MELLOR, G. L. 1980 Decaying turbulence in neutral and stratified fluids. *J. Fluid Mech.* **99**, 13–31.

FERNANDO, H. J. S. 1992 Mixing in stratified fluids. *Ann. Rev. Fluid Mech.* **23**, 455–493.

FINGER, J. E. & SCHMIDT, H. 1986 On the efficiency of different higher order turbulence models simulating the convective boundary layer. *Beitr. Z. Phys. Atmos.* **59**, 505–513.

GILBERT, B. 1980 Diffusion mixing in grid turbulence without mean shear. *J. Fluid Mech.* **100**, 349–365.

HAUGHDAL, J. & LIENHARD, V. J. H. 1988 A low cost high performance cold wire bridge. *J. Phys.* E **21**, 167.

HOPFINGER, E. J. 1987 Turbulence in stratified fluids: A review. *J. Geophys. Res.* **92**, 5287–5303.

HUNT, J. C. R. 1985 Diffusion in the stably stratified atmospheric boundary layer. *J. Climate Appl. Met.* **24**, 1187–1195.

JAYESH, YOON, K. & WARHAFT, Z. 1991 Turbulent mixing and transport in a thermally stratified interfacial layer in decaying grid turbulence. *Phys. Fluids* A **3**, 1143–1155.

JAYESH & WARHAFT, Z. 1992 Probability distribution, conditional dissipation, and transport of passive temperature fluctuations in grid-generated turbulence. *Phys. Fluids* A **4**, 2292–2307.

KOMORI, S. & UEDA, H. 1983 Turbulence structure in stably stratified open-channel flow. *J. Fluid Mech.* **130**, 13–26.

LINDEN, P. F. 1979 Mixing in stratified fluids. *Geophys. Astrophys. Fluid Dyn.* **13**, 3–23.

MA, B.-K. & WARHAFT, Z. 1986 Some aspects of the thermal mixing layer in grid turbulence. *Phys. Fluids* **29**, 3114–3120.

NIEUWSTADT, F. T. M. & VAN DOP, H. (ed.) 1982 *Atmospheric Turbulence and Air Pollution Modelling.* Reidel.

PHILLIPS, O. M. 1972 Turbulence in a strongly stratified fluid – is it unstable? *Deep-Sea Res.* **19**, 79–81.

POSMENTIER, E. S. 1977 The generation of salinity finestructure by vertical diffusion. *J. Phys. Oceanogr.* **7**, 298–300.

RILEY, J. J., METCALFE, R. W. & WEISSMANN, M. A. 1981 Direct numerical simulation of homogeneous turbulence in density-stratified fluids. In *Nonlinear Properties of Internal Waves* (ed. B. J. West). AIP *Conf. Proc.* vol. 76, pp. 79–112.

ROSS, S. 1988 *A First Course in Probability.* Macmillan.

RUDDICK, B. R., MCDOUGALL, T. J. & TURNER, J. S. 1989 The formation of layers in a uniformly stirred density gradient. *Deep-Sea Res.* **36**, 597–609.

SCHUMANN, U. 1987 The countergradient heat flux in turbulent stratified flows. *Nucl. Engng Design* **100**, 255–262.

STILLINGER, D. C., HELLAND, K. N. & VAN ATTA, C. W. 1983 Experiments on the transition of homogeneous turbulence to internal waves in a stratified fluid. *J. Fluid Mech.* **131**, 91–122.

TAVOULARIS, S. & CORRSIN, S. 1981 Experiments in nearly homogeneous turbulent shear flow with a uniform mean temperature gradient. Part 1. *J. Fluid Mech.* **104**, 311–347.

THORODDSEN, S. T. & VAN ATTA, C. W. 1992 Experimental tails and skewness of density-gradient probability density functions in stably stratified turbulence. *J. Fluid Mech.* **244**, 547–566.

THORODDSEN, S. T. & VAN ATTA, C. W. 1993 Experimental study of the effects of grid configuration on stably stratified grid-turbulence. *Dyn. Atmos. Oceans.*

TOWNSEND, A. A. 1976 *The Structure of Turbulent Shear Flow.* Cambridge University Press.

TURNER, J. S. 1973 *Buoyancy Effects in Fluids.* Cambridge University Press.

VEERAVALLI, S. & WARHAFT, Z. 1989 The shearless turbulence mixing layer. *J. Fluid Mech.* **207**, 191–229.

VEERAVALLI, S. & WARHAFT, Z. 1990 Thermal dispersion from a line source in the shearless turbulence mixing layer. *J. Fluid Mech.* **216**, 35–70.

VENKATRAM, A. & WYNGAARD, J. C. (ed.) 1988 *Air Pollution Modeling.* American Meteorological Society, Boston.

WYNGAARD, J. C. 1973 On surface layer turbulence. In *Workshop on Micrometeorology* (ed. D. A. Haugen), pp. 101–149.

YOON, K. & WARHAFT, Z. 1990 The evolution of grid-generated turbulence under conditions of stable thermal stratification. *J. Fluid Mech.* **215**, 601–638.

ZEMAN, O. & LUMLEY, J. L. 1976 Modeling buoyancy driven mixed layers. *J. Atmos. Sci.* **33**, 1974–1988.

ZEMAN, O. & TENNEKES, H. 1977 Parameterization of the turbulent energy budget at the top of the daytime atmospheric boundary layer. *J. Atmos. Sci.* **34**, 111–123.